

Antiferromagnetism in a Family of $S = 1$ Square Lattice Coordination Polymers $\text{NiX}_2(\text{pyz})_2$ ($X = \text{Cl}, \text{Br}, \text{I}, \text{NCS}$; $\text{pyz} = \text{Pyrazine}$)

Junjie Liu,[†] Paul A. Goddard,[‡] John Singleton,[§] Jamie Brambleby,[‡] Francesca Foronda,[†] Johannes S. Möller,[†] Yoshimitsu Kohama,[§] Saman Ghannadzadeh,[†] Arzhang Ardavan,[†] Stephen J. Blundell,[†] Tom Lancaster,^{||} Fan Xiao,^{||} Robert C. Williams,^{||} Francis L. Pratt,[⊥] Peter J. Baker,[⊥] Keola Wierschem,[#] Saul H. Lapidus,[▽] Kevin H. Stone,[○] Peter W. Stephens,[○] Jesper Bendix,[◆] Toby J. Woods,[¶] Kimberly E. Carreiro,[¶] Hope E. Tran,[¶] Cecelia J. Villa,[¶] and Jamie L. Manson^{*,¶}

[†]Department of Physics, Clarendon Laboratory, University of Oxford, Parks Road, Oxford OX1 3PU, United Kingdom

[‡]Department of Physics, University of Warwick, Gibbet Hill Road, Coventry, CV4 7AL, United Kingdom

[§]National High Magnetic Field Laboratory, Los Alamos National Laboratory, MS-E536, Los Alamos, New Mexico 87545, United States

^{||}Centre for Materials Physics, Durham University, South Road, Durham DH1 3LE, United Kingdom

[⊥]ISIS Pulsed Muon Facility, STFC Rutherford Appleton Laboratory, Chilton, Didcot, OX11 0QX, United Kingdom

[#]School of Physical and Mathematical Sciences, Nanyang Technological University, Singapore 637371, Singapore

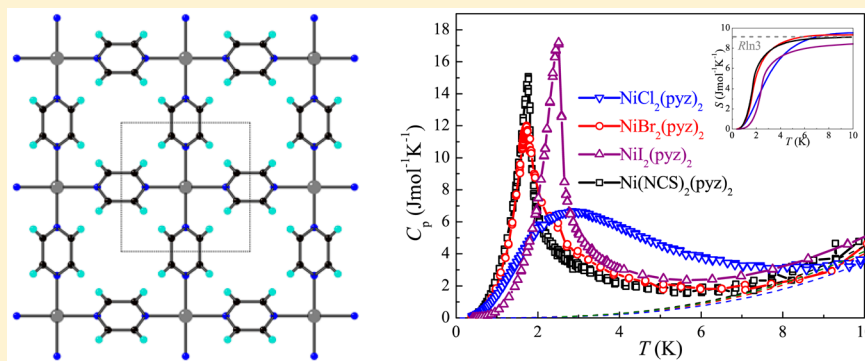
[▽]X-ray Science Division, Advanced Photon Source, Argonne National Laboratory, Lemont, Illinois 60439, United States

[○]Department of Physics and Astronomy, State University of New York, Stony Brook, New York 11794, United States

[◆]Department of Chemistry, University of Copenhagen, Copenhagen DK-2100, Denmark

[¶]Department of Chemistry and Biochemistry, Eastern Washington University, Cheney, Washington 99004, United States

S Supporting Information



ABSTRACT: The crystal structures of $\text{NiX}_2(\text{pyz})_2$ ($X = \text{Cl}$ (1), Br (2), I (3), and NCS (4)) were determined by synchrotron X-ray powder diffraction. All four compounds consist of two-dimensional (2D) square arrays self-assembled from octahedral NiX_4 units that are bridged by pyz ligands. The 2D layered motifs displayed by 1–4 are relevant to bifluoride-bridged $[\text{Ni}(\text{HF}_2)(\text{pyz})_2]\text{EF}_6$ ($E = \text{P}, \text{Sb}$), which also possess the same 2D layers. In contrast, terminal X ligands occupy axial positions in 1–4 and cause a staggered packing of adjacent layers. Long-range antiferromagnetic (AFM) order occurs below 1.5 (Cl), 1.9 (Br and NCS), and 2.5 K (I) as determined by heat capacity and muon-spin relaxation. The single-ion anisotropy and g factor of 2, 3, and 4 were measured by electron-spin resonance with no evidence for zero-field splitting (ZFS) being observed. The magnetism of 1–4 spans the spectrum from quasi-two-dimensional (2D) to three-dimensional (3D) antiferromagnetism. Nearly identical results and thermodynamic features were obtained for 2 and 4 as shown by pulsed-field magnetization, magnetic susceptibility, as well as their Néel temperatures. Magnetization curves for 2 and 4 calculated by quantum Monte Carlo simulation also show excellent agreement with the pulsed-field data. Compound 3 is characterized as a 3D AFM with the interlayer interaction (J_{\perp}) being slightly stronger than the intralayer interaction along Ni-pyz-Ni segments (J_{pyz}) within the two-dimensional $[\text{Ni}(\text{pyz})_2]^{2+}$ square planes. Regardless of X , J_{pyz} is similar for the four compounds and is roughly 1 K.

Received: December 30, 2015

1. INTRODUCTION

Low-dimensional Ni(II)-based $S = 1$ quantum antiferromagnetic nets continue to draw much interest from the condensed matter science community. Since Haldane^{1,2} predicted that an antiferromagnetic Heisenberg chain has a singlet ground state and a finite gap to the lowest excited state for integer spins, this conjecture has inspired numerous studies of $S = 1$ antiferromagnets in low dimensions. While most of the work done so far is related to one-dimensional (1D) models or quasi-one-dimensional (Q1D) compounds,^{3–11} less work has been performed on two-dimensional models (2D) or quasi-two-dimensional (Q2D) compounds^{12–15} partially due to the difficulty in applying theoretical/numerical techniques to these models. In low-dimensional $S = 1$ antiferromagnets, the nature of the ground state can be strongly modified by the spatial dimensionality as well as the zero-field splitting (ZFS) of $3d^8$ Ni(II),¹⁶ both of which can be tuned by chemical synthesis. In addition, the presence of two orthogonal magnetic orbitals in octahedrally coordinated Ni(II), d_{z^2} and $d_{x^2-y^2}$, affords multiple options for forming spin exchange pathways, allowing flexibility in tuning the magnetic dimensionality via crystal engineering.

We and others have been developing two-dimensional Cu(II)-based square lattices comprised of pyrazine (pyz) bridges. Among these are $[\text{Cu}(\text{HF}_2)(\text{pyz})_2]\text{Z}$ ($\text{Z} = \text{BF}_4^-$, PF_6^- , SbF_6^- and TaF_6^-),^{17–20} $[\text{Cu}(\text{ClO}_4)_2(\text{pyz})_2]$,^{21,22} $[\text{Cu}(\text{BF}_4)_2(\text{pyz})_2]$,²³ and $[\text{Cu}(\text{pyz})_2(\text{pyO})_2](\text{PF}_6)_2$,²⁴ which all display long-range order (LRO) between 1.5 and 4.3 K. The square $[\text{Cu}(\text{pyz})_2]^{2+}$ planes in $[\text{Cu}(\text{HF}_2)(\text{pyz})_2]\text{Z}$ are connected by HF_2^- bridges to afford three-dimensional (3D) frameworks with Z occupying the interior sites. However, the magnetism is very two-dimensional as a result of very weak couplings through Cu–FHF–Cu bonds²⁵ due to limited overlap between the fluorine p_z orbital and the magnetic orbital of Cu(II), $d_{x^2-y^2}$, lying in the $[\text{Cu}(\text{pyz})_2]^{2+}$ planes.²⁶ The last three examples above contain axial ClO_4^- , BF_4^- , or pyO ligands, and the 2D layers stack in a staggered fashion. Extension of some of this work to include Ni(II) has proven to be more challenging, as growth of single crystals is difficult. As such, implementation of synchrotron X-ray diffraction to determine crystal structures, including those described here, has been crucial to our characterization efforts. In addition, the $^3\text{A}_g$ ground state of an octahedrally coordinated Ni(II) ion is magnetically more complex than Cu(II) owing to the presence of ZFS induced by spin–orbital couplings. The effective spin Hamiltonian ($S = 1$) is given by

$$\hat{H} = \sum_{(i)} D(\hat{S}_i^{z^2}) + \sum_{(i,j)} J_{ij} \hat{S}_i \cdot \hat{S}_j \quad (1)$$

Experimentally, it becomes challenging to distinguish between the effects from magnetic exchange interactions (J_{ij}) and single-ion ZFS (D), especially when polycrystalline samples are involved.²⁷ The difficulty lies in the fact that, in many circumstances, magnetometry data can be fitted to several models with different combinations of D and J , which makes it challenging to characterize a system unambiguously. In such a case, additional spectroscopic measurements are required to constrain the parameters in the Hamiltonian.

Considering these challenges, we recently described the structural, electronic and magnetic properties of $[\text{Ni}(\text{HF}_2)(\text{pyz})_2]\text{Z}$ ($\text{Z} = \text{PF}_6^-$, SbF_6^-).^{27,28} Interestingly, $\text{Z} = \text{PF}_6^-$ exists as two isolable polymorphs with similar 3D structural motifs; the α -phase is monoclinic, while the β -phase is tetragonal and isostructural to the equivalent Cu(II) compound. A spatial

exchange anisotropy was found in these materials due to the presence of coexisting Ni–FHF–Ni (J_{FHF}) and Ni–pyz–Ni pathways (J_{pyz}), where $J_{\text{FHF}} > J_{\text{pyz}}$. The dominant Ni–FHF–Ni pathways allowed us to interpret the $\chi(T)$ data according to a Q1D chain model above T_{max} but it was not possible to experimentally determine J_{pyz} owing to the polycrystalline nature of the samples. Density-functional theory (DFT) confirmed the magnetic exchange properties of these systems and that J_{pyz} was indeed much smaller than J_{FHF} . Angular overlap model (AOM) analyses of UV–vis spectroscopic data determined D to be -7.5 K (α - PF_6^-), 10.3 K (β - PF_6^-), and 11.2 K (SbF_6^-).²⁷ The correspondingly high Néel temperatures (T_{N} , the onset of long-range antiferromagnetic order) of 6.2, 7.0, and 12.2 K suggest that J_{pyz} must be larger than that calculated, or alternatively, the magnetic orders are assisted by D . In order to address these scenarios as well as to find J_{pyz} quantitatively, analogous model compounds based on weakly interacting 2D $[\text{Ni}(\text{pyz})_2]^{2+}$ square lattices are required for comparison.

Four compounds with similar $[\text{Ni}(\text{pyz})_2]^{2+}$ square lattices were synthesized and studied: $\text{NiCl}_2(\text{pyz})_2$ (**1**), $\text{NiBr}_2(\text{pyz})_2$ (**2**), $\text{NiI}_2(\text{pyz})_2$ (**3**), and $\text{Ni}(\text{NCS})_2(\text{pyz})_2$ (**4**). Some of them, notably **1**, **2**, and **4**, were synthesized and spectroscopically characterized several years ago,^{29–32} although their crystal structures were not explicitly determined. More recently, the structure of **2** was determined by powder neutron diffraction and found to be consistent with the hypothetical square lattice structure.³³ Compound **3** is described here for the first time. The related Ni(II) compound, **4**, reportedly exists in two polymorphic forms; however, as will be described below, we find evidence for only one of the two phases in our samples.^{34,35}

As for the magnetic properties of **1–4**, the temperature dependence of the magnetic susceptibility data, $\chi(T)$, for **1** and **2** have been reported ($T \geq 5$ K),^{32,33} while those for **3** and **4** have not. The analysis of the $\chi(T)$ data for **1** and **2** gave $D = 7.92$ and 14.8 K, respectively. Furthermore, these studies also suggested that magnetic couplings along Ni–pyz–Ni were probably very weak. An estimate of J_{pyz} was made by employing a mean-field contribution, giving $zJ = 0.39$ K for **1** and 0.95 K for **2**.^{32,33}

In this work, we have carried out an extensive experimental and theoretical investigation of **1–4**, employing modern instrumental methods to characterize their structural as well as temperature- and field-dependent magnetic properties. Our interpretation of the experimental results suggests the interlayer magnetic couplings in **1–4** are significantly suppressed compared to the $[\text{Ni}(\text{HF}_2)(\text{pyz})_2]\text{Z}$ compounds and become comparable or less than J_{pyz} . To clarify the possible Ni(II) ZFS contribution to the magnetism, electron spin resonance (ESR) experiments were performed on **1–4**. J_{pyz} in **2–4** is quantitatively determined within the picture of Q2D magnetism, and the conclusions are supported by quantum Monte Carlo (QMC) calculations. The common $[\text{Ni}(\text{pyz})_2]^{2+}$ square lattices exhibited by **1–4** are relevant to establishing magnetostructural correlations in the metal–organic frameworks, $[\text{Ni}(\text{HF}_2)(\text{pyz})_2]\text{Z}$ ($\text{Z} = \text{PF}_6^-$ and SbF_6^-).

2. EXPERIMENTAL METHODS

Syntheses. Following a general procedure, **1** and **2** were prepared as powders using a fast precipitation reaction between the corresponding $\text{NiX}_2 \cdot y\text{H}_2\text{O}$ and two equivalents of pyrazine. Each reagent was dissolved in 3 mL of H_2O and quickly mixed together while stirring. For **4**, KNCS (2.16 mmol, 0.2100 g) and pyz (2.16 mmol, 0.1730 g) were dissolved together in 5 mL of H_2O . To this solution was added, while stirring, $\text{Ni}(\text{NO}_3)_2 \cdot y\text{H}_2\text{O}$ (1.08 mmol, 0.1973 g) to afford a pale blue precipitate.

In all instances, the powders were isolated by suction filtration, washed with H_2O , and dried in vacuo for ~ 2 h. Compound **3** was prepared via a mechanochemical reaction involving grinding of NiI_2 (2.88 mmol, 0.9013 g) with an excess of pyrazine (6.78 mmol, 0.2307 g). A Parr acid-digestion bomb was charged with the reaction mixture and placed inside a temperature programmable oven which was set at a temperature of 403 K. The sample was held isothermal for 2 weeks and then allowed to cool slowly to room temperature, at which time a homogeneous orange-brown solid had formed. The final product was obtained by washing the sample with fresh diethyl ether to remove any unreacted pyz. All four compounds were highly pure and isolated in yields exceeding 90%.

Structural Determinations. For $\text{NiX}_2(\text{pyz})_2$ ($X = \text{Cl}$, Br or NCS), high resolution synchrotron powder X-ray diffraction patterns were collected at the X12A and X16C beamline at the National Synchrotron Light Source at Brookhaven National Laboratory. X-rays of a particular wavelength were selected using a $\text{Si}(111)$ channel cut monochromator. Behind the sample, the diffracted beam was analyzed with a $\text{Ge}(111)$ crystal and detected by a NaI scintillation counter. Wavelength and diffractometer zero were calibrated using a sample of NIST Standard Reference Material 1976, a sintered plate of Al_2O_3 . The sample was loaded into a 1.0-mm-diameter glass capillary and flame-sealed.

For $\text{NiI}_2(\text{pyz})_2$, high resolution synchrotron powder X-ray diffraction data were collected using beamline 11-BM at the Advanced Photon Source (APS).³⁶ Discrete detectors are scanned over a 34° range in 2θ with data points collected every 0.001° using a scan speed of $0.01^\circ/\text{s}$. Data were collected while continually scanning the diffractometer 2θ -arm.

Indexing was performed in TOPAS Academic,^{37,38} and space groups were tentatively assigned through systematic absences to be $I4/mmm$ for $\text{NiX}_2(\text{pyz})_2$ ($X = \text{Cl}$, Br , or I) and $C2/m$ for $\text{Ni}(\text{NCS})_2(\text{pyz})_2$. The $I4/mmm$ space group was also reported for $\text{NiBr}_2(\text{pyz})_2$ in ref 33. From the space group assignment and stoichiometric contents, it was possible to place the Ni on the corresponding $2a$ (0, 0, 0) special position. The remaining atomic positions were determined by simulated annealing in TOPAS Academic. From these initial models, these structures were successfully refined to determine more precise atomic positions. Pyrazine hydrogens were placed on ideal geometrically determined positions.

Magnetic Measurements. Magnetization (M) versus temperature data were collected (and converted to susceptibility by the relation $\chi(T) = M/H$) on a Quantum Design MPMS 7 T SQUID. Powder samples of **1–4** were loaded into gelatin capsules, mounted in a plastic drinking straw, and affixed to the end of a stainless steel/brass rod. The sample was cooled in zero-field to a base temperature of 2 K, the magnet charged to 0.1 T, and data taken upon warming to 300 K.

Pulsed Fields. $M(B)$ measurements (up to 60 T) made use of a 1.5-mm-bore, 1.5-mm-long, 1500-turn-compensated coil susceptometer, constructed from a 50 gauge high-purity copper wire. When the sample is within the coil, the signal voltage V is proportional to dM/dt , where t is the time. Numerical integration of V is used to evaluate M . The sample is mounted within a 1.3-mm-diameter ampule that can be moved in and out of the coil. Accurate values of M are obtained by subtracting empty coil data from that measured under identical conditions with the sample present. The susceptometer was placed inside a ^3He cryostat providing a base temperature of 0.5 K. The field B was measured by integrating the voltage induced in a 10-turn coil calibrated by observing the de Haas–van Alphen oscillations of the belly orbits of the copper coils of the susceptometer.

Heat Capacity. C_p measurements were carried out on polycrystalline samples of **1–4** by means of two independent techniques; the traditional relaxation³⁹ and dual-slope methods.⁴⁰ In the relaxation method, the heat pulse was applied to the sample heater, and the resultant exponential temperature decay with a small temperature step, which is $\sim 3\%$ of the thermal bath temperature, was observed. The C_p at a single temperature was evaluated by the time constant of the decay curve and the thermal conductance of the thermal link. In the dual slope method, the sample was heated and subsequently cooled through a broad temperature range, and the $C_p(T)$ in the wide temperature range was evaluated using both heating and cooling curves. This method

allows quick collection of a large amount of $C_p(T)$ data, which is important in determining the transition temperature at several magnetic fields. However, it requires an excellent thermal contact between the sample and the thermometer that can only be used in cases of minimal tau-2 effects; i.e., the thermal relaxation between the sample and the platform must be fast.⁴⁰ For this reason, $C_p(T)$ of **1** was obtained by traditional relaxation method only. For **4**, using the same setup as the experiments, we additionally observed a magnetocaloric effect (MCE) by sweeping the magnetic field at 1 T/min. This method measures the entropy change as a function of magnetic field and can detect phase boundaries with cooling and heating responses.⁴¹ These $C_p(T)$ and MCE measurements were performed on 2.910, 1.479, 2.284, and 0.3406 mg of **1**, **2**, **3**, and **4**, respectively. The powders were mixed with a small amount of Apiezon-N grease and pressed between Si plates to obtain good temperature homogeneity. Compounds **1**, **2**, and **4** were measured in an Oxford 15 T superconducting magnet system capable of reaching a base temperature of 0.4 K. Compound **3** was measured in a 9 T Quantum Design Physical Property Measurement System. The addenda specific heats due to Apiezon-N grease, Si plates, and sample platform were measured separately. After subtracting the addenda contribution from the total specific heat, the specific heat of the sample was obtained. Excellent agreement (within $\sim 5\%$) between the two $C_p(T)$ techniques was confirmed for **2** and **4**.

Muon-Spin Relaxation. Zero-field muon-spin relaxation (ZF μSR) measurements were made on polycrystalline samples of **1–4** using the general purpose surface (GPS) spectrometer at the Swiss Muon Source (**1** and **2**) and the EMU (**1**), MuSR (**3**), and ARGUS (**4**) instruments at the STFC ISIS facility. For the measurement, the samples were mounted in silver foil packets onto silver backing plates.

In a μSR experiment,⁴² spin-polarized positive muons are stopped in a target sample, where the muon usually occupies an interstitial position in the crystal. The observed property in the experiment is the time evolution of the muon spin polarization, the behavior of which depends on the local magnetic field at the muon site. Each muon decays, with an average lifetime of $2.2 \mu\text{s}$, into two neutrinos and a positron, the latter particle being emitted preferentially along the instantaneous direction of the muon spin. Recording the time dependence of the positron emission directions therefore allows the determination of the spin-polarization of the ensemble of muons. In our experiments, positrons are detected by detectors placed forward (F) and backward (B) of the initial muon polarization direction. Histograms $N_F(t)$ and $N_B(t)$ record the number of positrons detected in the two detectors as a function of time following the muon implantation. The quantity of interest is the decay positron asymmetry function, defined as

$$A(t) = \frac{N_F(t) - \alpha_{\text{exp}} N_B(t)}{N_F(t) + \alpha_{\text{exp}} N_B(t)} \quad (2)$$

where α_{exp} is an experimental calibration constant. $A(t)$ is proportional to the spin polarization of the muon ensemble.

Electron Spin Resonance (ESR). D-band (130 GHz) ESR measurements were performed on powder samples of **1–3**. A phase-locked dielectric resonator oscillator in conjunction with a series of IMPATT diodes was used as the microwave source and detector. A field modulation was employed for D-band ESR measurements. Multi-high-frequency EPR measurements were also performed on a powder sample of **2–4** using a cavity perturbation technique spanning the frequency range from 40 to 170 GHz. A millimeter-vector-network analyzer served as the microwave source and detector. ESR measurements were performed in a 6 T horizontal-bore superconducting magnet with the temperature regulated between 1.5 and 300 K using a helium gas flow cryostat.

Quantum Monte Carlo Calculations. Numerical calculations of the spin-1 antiferromagnetic Heisenberg model in an applied magnetic field were performed using the stochastic series expansion quantum Monte Carlo (QMC) method with directed loop updates.⁴³ For antiferromagnetic exchange interactions, sublattice rotation is required to avoid the sign problem in QMC. By taking the direction of the applied magnetic field as the discretization axis, sublattice rotation on a bipartite lattice leads to a sign-problem-free Hamiltonian as long as the applied

Table 1. Crystallographic Refinement Parameters for 1–4 As Determined by Synchrotron X-Ray Powder Diffraction

compound	NiCl ₂ (pyz) ₂ (1)	NiBr ₂ (pyz) ₂ (2)	NiI ₂ (pyz) ₂ (3)	Ni(NCS) ₂ (pyz) ₂ (4)
emp. formula	C ₈ N ₄ H ₈ NiCl ₂	C ₈ N ₄ H ₈ NiBr ₂	C ₈ N ₄ H ₈ NiI ₂	C ₁₀ N ₆ H ₈ NiS ₂
wt. (g/mol)	289.77	378.67	472.68	335.03
T (K)	298	298	100	298
crystal class	tetragonal	tetragonal	tetragonal	monoclinic
space group	I4/mmm	I4/mmm	I4/mmm	C2/m
a (Å)	7.0425(2)	7.0598(2)	7.057502(18)	9.9266(2)
b (Å)	7.0425(2)	7.0598(2)	7.057502(18)	10.2181(2)
c (Å)	10.7407(3)	11.3117(3)	12.25594(5)	7.2277(2)
β (deg)	90	90	90	118.623(2)
V (Å ³)	532.71(3)	563.79(4)	610.448(5)	643.52(3)
Z	2	2	2	2
ρ (g/cm ³)	1.807	2.231	2.571	1.729
λ (Å)	0.699973	0.754056	0.41374	0.6984
R _{wp}	0.05592	0.04524	0.04648	0.04531
R _{exp}	0.06987	0.05449	0.03249	0.05644
X	1.471	1.093	1.431	1.720

field is parallel or perpendicular to the axis of exchange anisotropy. The case of applied field parallel to the axis of exchange anisotropy has been well-studied. For the case of perpendicular applied fields, we use a slightly modified approach to account for a lack of the usual conservation law.⁴⁴

Density Functional Theory (DFT). Computational modeling was performed on dinuclear entities using the structural data from X-ray determinations. Evaluation of the exchange couplings was based on the broken-symmetry (BS) approach of Noodleman⁴⁵ as implemented in the ORCA version 2.8 suite of programs.^{46–48} The formalism of Yamaguchi et al., which employs calculated expectation values $\langle S^2 \rangle$ for both high-spin and broken-symmetry states, was used.^{49,50} Calculations related to magnetic interactions have been performed using the PBE0 functional. The def2-TZVP basis function set from Ahlrichs was used.⁵¹

3. RESULTS

A. Crystal Structures. Crystallographic refinement details as well as selected bond lengths and bond angles for 1–4 are listed in Tables 1 and 2. The data correspond to room temperature (1, 2, and 4) and 100 K (3) structures.

NiCl₂(pyz)₂ (1), NiBr₂(pyz)₂ (2), and NiI₂(pyz)₂ (3). The atom labeling scheme is shown in Figure 1a. Compounds 1–3 are isomorphous and consist of tetragonally elongated NiX₂N₄ sites, with the axial sites being occupied by the bulkier X anions. The Ni–N distances are only slightly perturbed by X [2.145(2) Å (1), 2.131(4) Å (2), and 2.133(1) Å (3)], whereas the Ni–X bond lengths are substantially longer at 2.400(1) Å (1), 2.5627(9) Å (2), and 2.7919(1) Å (3) due to increasing ionic radius of the halide. The Ni–N distances in 1–3 are similar to those reported in other compounds with Ni–pyz–Ni bridges.^{27,28,33,35} However, the axial bonds (Ni–X) in 1–3 are significantly longer than those in compounds with related structures that contain either 1D or 2D Ni–pyz–Ni bridges. This is likely due to the relatively large radius of the halogen atoms in 1–3 comparing the axial ligands in other systems which contain smaller O- or N-donor atoms. The topological structures of 1–3 can be described as infinite 2D square lattices with NiX₂N₄ octahedra bridged by pyz linkages along the *a* and *b* axes (Figure 2a) to afford perfectly linear Ni–N⋯N trajectories.

A 2-fold positional disorder of the pyz ligands occurs as a result of the mirror planes in the *I4/mmm* space group (Figure 2b). The small unit cell is consistent with this disorder. To have an ordered arrangement such that adjacent pyz ligands adopt a propeller-like disposition around the Ni(II) center would require a larger unit

Table 2. Selected Bond Lengths (Å) and Bond Angles (deg) for 1–4

NiCl ₂ (pyz) ₂ (1)			
Ni1–N1	2.145(2)	Ni1–Cl1	2.400(1)
N1–C1	1.336(2)	N1–Ni1–Cl1	90°
Cl1–Ni1–Cl1	180°	N1–Ni1–N1	90°
Ni1–N1–C1	120.5(1)°	dihedral angle ^a	47.4(2)°
NiBr ₂ (pyz) ₂ (2)			
Ni1–N1	2.131(4)	Ni1–Br1	2.5627(9)
N1–C1	1.351(1)	N1–Ni1–Br1	90°
Br1–Ni1–Br1	180°	N1–Ni1–N1	90°
Ni1–N1–C1	121.4(2)°	dihedral angle ^a	46.5(2)°
NiI ₂ (pyz) ₂ (3)			
Ni1–N1	2.133(1)	Ni1–I1	2.7919(9)
N1–C1	1.349(1)	N1–Ni1–I1	90°
I1–Ni1–I1	180°	N1–Ni1–N1	90°
Ni1–N1–C1	121.4(2)°	dihedral angle ^a	45.8(1)°
Ni(NCS) ₂ (pyz) ₂ (4)			
Ni1–N1	2.020(5)	Ni1–N2	2.184(3)
N1–C1	1.184(7)	N2–C2	1.303(3)
S1–C1	1.591(5)	C2–C3	1.401(5)
N1–C2–S1	175.5(7)°	N1–N1–C1	163.3(5)°
N1–Ni1–N2	88.4(2)°	N1–Ni1–N1	180°
N2–Ni1–N2	180°	dihedral angle ^a	65.3(2)°

^aMeasured as the pyz tilt angle relative to the *ab*-plane.

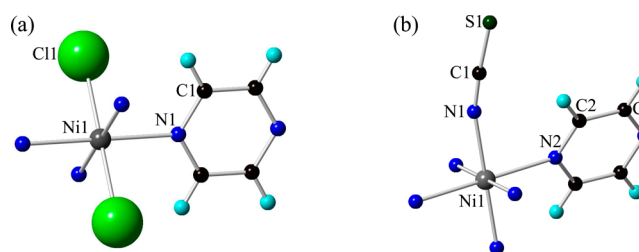


Figure 1. Room temperature asymmetric units and atom labeling schemes for (a) NiCl₂(pyz)₂ (1) and (b) Ni(NCS)₂(pyz)₂ (4). The asymmetric units and atom labeling schemes for NiBr₂(pyz)₂ (2) and NiI₂(pyz)₂ (3) are similar to those of 1 with the Cl atom being replaced by Br and I for 2 and 3, respectively.

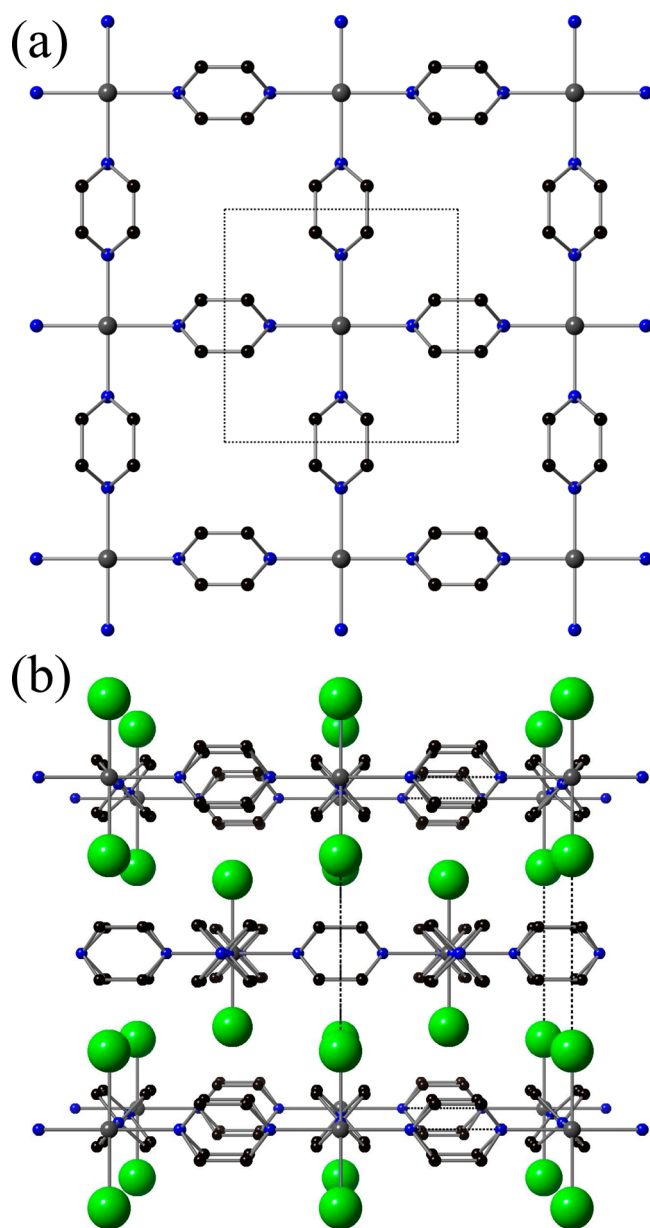


Figure 2. (a) Two-dimensional layer of $\text{NiCl}_2(\text{pyz})_2$ (**1**) with axial Cl atoms omitted for clarity. (b) Staggered packing of 2D layers in **1**. The positional disorder of the pyz ligands is shown as double pyz rings connecting Ni atoms. $\text{NiBr}_2(\text{pyz})_2$ (**2**) and $\text{NiI}_2(\text{pyz})_2$ (**3**) are isostructural with **1**. The unit cell is indicated by dashed lines. Ni, Cl, N, and C atoms are represented as gray, green, blue, and black spheres, respectively. H atoms are omitted for clarity.

cell of nominal size $\sqrt{2}a \times \sqrt{2}a \times c$ or perhaps $\sqrt{2}a \times \sqrt{2}a \times 2c$ and likely be primitive as observed for $[\text{Ni}(\text{HF}_2)(\text{pyz})_2]\text{SbF}_6$ ($P4/nmm$).²⁷ The presence of a supercell would result in weak superlattice reflections, none of which were detected by our synchrotron X-ray experiments. A similar pyz disorder has been reported in $\text{Ni}(\text{NCO})_2(\text{pyz})_2$, which possesses identical $I4/mmm$ symmetry.³⁵ In **1–3**, the canting angles at which the pyz rings are tilted about their N–N axes with respect to the ab plane are very similar (47.4° , 46.5° , and 45.8° for **1**, **2**, and **3**, respectively) although significantly less than that found in **4** (65.3°).

The $[\text{Ni}(\text{pyz})_2]^{2+}$ layers stack along the c direction such that the Ni(II) ion of a given lattice lies above/below the centers of

neighboring square lattices (Figure 2b). The bulky X anions act as spacers to separate each layer, giving interlayer Ni⋯Ni separations of 7.32 Å (**1**), 7.54 Å (**2**), and 7.90 Å (**3**). It should be noted that the 2D structural motif was anticipated based on early infrared spectroscopic evidence^{31,32} and now confirmed here using X-ray structural data.

It is worth mentioning that two structures were previously reported for the Co-congener of **1**, $\text{CoCl}_2(\text{pyz})_2$. The far-infrared spectra for $\text{CoCl}_2(\text{pyz})_2$ suggested tetragonal symmetry ($I4/mmm$),⁵² whereas a later single crystal X-ray study indicated an orthorhombic space group $Ccca$.⁵³ Both structures consist of a square lattice motif with Co(II) centers bridged by pyz ligands. For the sake of comparison, the high-intensity synchrotron diffraction data for **1–3** were also fitted against the $Ccca$ space group, but poor agreement was found as several calculated intensities were either split or completely missing from the experimental data. A similar detailed structural study of **2** also indicated preference for $I4/mmm$.³³ From our work, we conclude that the $I4/mmm$ space group is the appropriate choice for these materials, at least, as prepared using our synthetic methodology.

$\text{Ni}(\text{NCS})_2(\text{pyz})_2$ (**4**). Previously, two different structural modifications have been reported, each having monoclinic symmetry ($C2/m$ and $P2_1/n$) at 293 K.^{34,35} Although both structures possess octahedral Ni(II) centers, four pyz ligands in the equatorial plane, two axial NCS^- ligands and 2D layered motifs that consist of orthogonally cross-linked Ni–pyz–Ni chains, an essential difference between them lies in the relative distortion of the NiN_6 octahedron. In the $C2/m$ structure as described by Wriedt et al.,³⁴ four equivalent Ni– N_{pyz} bonds [$2.162(1)$ Å] occupy the 2D plane while the axial direction contains shorter Ni–N bonds [$2.033(2)$ Å]. In contrast, three distinct pairs of Ni–N distances are found in the $P2_1/n$ variant, with an axial elongation along one of the Ni–pyz–Ni chains [$\text{Ni–N}_{\text{pyz}} = 2.440(3)$ Å]. The other two Ni–N bonded pairs contain the other (orthogonal) Ni–pyz–Ni chain, whereas the Ni–N bonds (from the NCS^- ligand) are $1.945(3)$ Å. The strong elongation of the six-coordinate Ni(II) center is at odds with expectations especially since Jahn–Teller distortion is not possible for a $3d^8$ ion.

For the sake of a careful structural and magnetic comparison to **1–3**, we have re-examined the 298 K structure of **4** using high-resolution synchrotron powder X-ray diffraction. We found the crystal structure of **4** to be essentially identical to that of the reported $C2/m$ phase and describe the structure in detail here as it is pertinent to the development of magnetostructural correlations.

Indeed, **4** features four equivalent Ni–N2 (from pyz) bond distances of $2.184(3)$ Å while Ni–N1 (from NCS^-) bonds are shorter at $2.020(5)$ Å. These Ni–N distances are significantly different to the $P2_1/n$ phase. Other striking variations are observed in the bond angles about the NiN_6 octahedron. The main structural feature of **4** is the planar 2D nearly square grid that propagates in the ab plane as illustrated in Figure 3a. Here, adjoining orthogonal chains afford equivalent intralayer Ni⋯Ni separations of $7.123(1)$ Å along both Ni–pyz–Ni chains. The square exhibits a slight rhombic distortion such that the diagonals vary by 3% (9.926 vs 10.218 Å). Also of importance is that the pyz ligands form slightly nonlinear Ni–pyz–Ni bridges such that the N-donor atoms (N1) of the pyz ring lie just off the Ni⋯Ni trajectory. The Ni1–N2⋯Ni1 backbone has an angle of 177.3° as compared to the 180° angles found in **1–3**. By comparison, the $P2_1/n$ structure exhibits inequivalent Ni⋯Ni distances of $6.982(1)$ Å along the a axis and $7.668(2)$ Å along b .

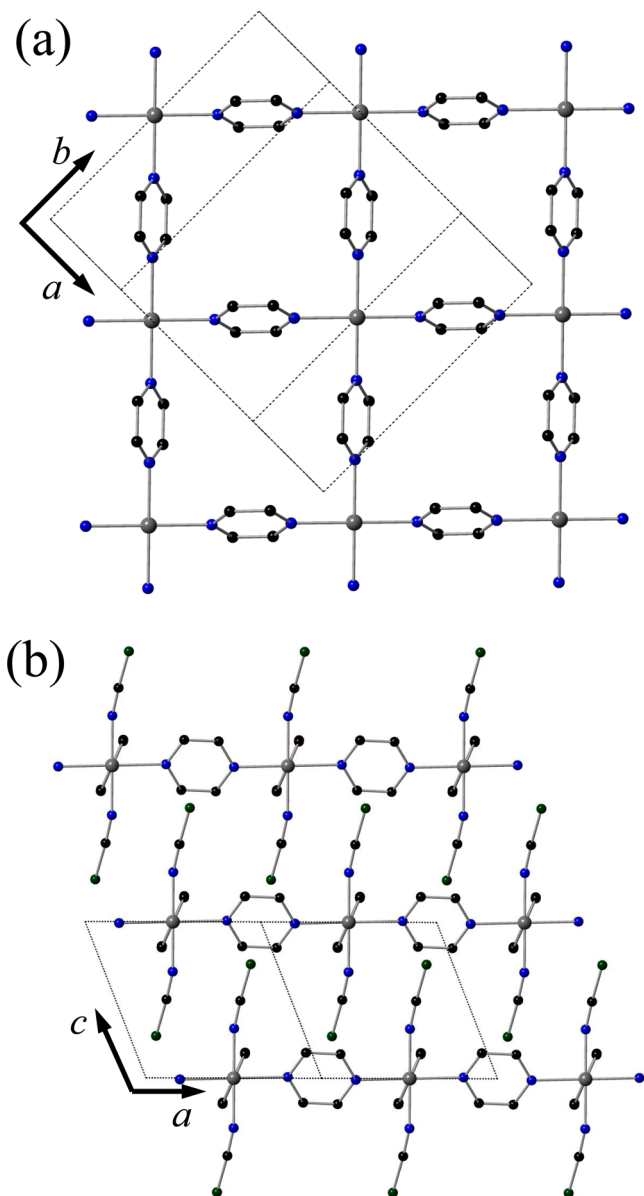


Figure 3. Crystal structure of $\text{Ni}(\text{NCS})_2(\text{pyz})_2$ (**4**). (a) A 2D sheet viewed normal to the ab plane where the slight rhombic distortion of the sheet is readily seen. NCS ligands are omitted for clarity. (b) Staggered packing of sheets. The unit cell is indicated by dashed lines. Ni, S, N, and C atoms are represented as gray, dark green, blue, and black spheres, respectively. H atoms are omitted for clarity.

The 2D layers in **4** are staggered such that the axial NCS^- ligands protrude toward the midpoints of adjacent layers; they stack perpendicular to the c axis (Figure 3b). The closest interlayer $\text{Ni}\cdots\text{Ni}$ separation is $7.2277(2)$ Å, which corresponds to the c axis repeat unit.

An isomorphous series of compounds exists, $M(\text{NCS})_2(\text{pyz})_2$ where $M = \text{Mn, Fe, Co, and Ni}$.^{54–56} The $\text{Cu}(\text{II})$ ion forms $\text{Cu}(\text{NCS})_2(\text{pyz})_2$, which contains 2D rectangular layers made up of bi-bridged $\text{Cu}-(\text{NCS})_2-\text{Cu}$ ribbons that are cross-linked via pyz bridges.⁵⁷ Substitution of 4,4'-bipyridine (4,4'-bipy) for pyz affords the related structure $\text{Cu}(\text{NCS})_2(4,4'\text{-bipy})$.⁵⁸

B. Search for Long-Range Magnetic Order by Heat Capacity. Figure 4 displays the zero-field heat capacity (C_p) of compounds **1–4** collected in the temperature range of 0.4–10 K. λ anomalies centered at 1.8(1), 2.5(1), and 1.8(1) K were

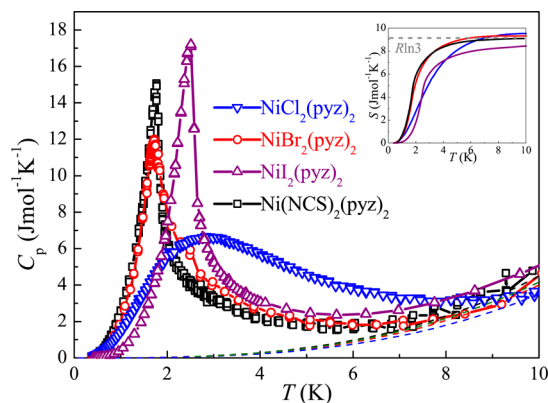


Figure 4. Specific heat of polycrystalline samples of $\text{NiX}_2(\text{pyz})_2$ ($X = \text{Cl}$ (**1**), Br (**2**), I (**3**), and NCS (**4**)). Main panel: zero field heat capacity data collected between 1 and 10 K. The dash lines represent the estimated lattice contribution C_{latt} . Inset: the temperature dependence of the magnetic entropy for **1–4**.

observed in the C_p curves for $\text{NiBr}_2(\text{pyz})_2$ (**2**), $\text{NiI}_2(\text{pyz})_2$ (**3**), and $\text{Ni}(\text{NCS})_2(\text{pyz})_2$ (**4**), respectively. The lattice contributions (C_{latt}) to heat capacities are calculated by fitting the C_p at high temperatures (>10 K) using a simple Debye fitting.²⁸ After subtracting the lattice contribution, the temperature dependence of magnetic entropy is calculated as shown in the inset to Figure 4, which exhibits the tendency to saturate to $R \ln 3$ for all four compounds. This suggests that the C_p anomaly stems from the $S = 1$ spin [$\text{Ni}(\text{II})$ ions] for **1–4**.

The distinct C_p anomalies for **2–4** are attributed to the antiferromagnetic (AFM) LRO of $S = 1$ spins. In low-dimensional antiferromagnets with strong spatial exchange anisotropy, λ peaks are suppressed due to the onset of short-range ordering above T_N , which reduces the entropy change at the transition to LRO.⁵⁹ The presence of the λ peaks indicates that **2–4** are close to 3D antiferromagnets in which the interactions in all directions, i.e., within and between the $[\text{Ni}(\text{pyz})_2]^{2+}$ layers, are similar. On the other hand, the C_p for $\text{NiCl}_2(\text{pyz})_2$ (**1**) shows no sharp peak over the measured T range. The broad C_p peak in **1** can be explained by the thermal excitation among $S = 1$ spin states (Schottky anomaly) and/or low-dimensional spin correlations. Unfortunately, we could not draw an unambiguous conclusion as to the sign or magnitude of D for **1**. However, the hypothesized D value (based on ESR and susceptibility measurements) is significantly larger than the exchange interaction between $\text{Ni}(\text{II})$ ions (see below). Therefore, the thermal excitation among the $S = 1$ multiplet is expected to have marked contributions to the magnetic heat capacity of **1** at high temperatures. The magnetic contribution (C_{mag}) to the heat capacity for **1** is calculated by subtracting C_{latt} from C_p as shown in Figure 5a. Below 0.6 K, C_{mag} can be fitted to the spin-wave excitation, $C_{\text{mag}} \propto T^{d/n}$, with $d = 2.99(3)$ and $n = 1$ as shown in the inset to Figure 5a. This temperature dependence deviates from that expected for the Schottky anomaly ($C_{\text{mag}} \propto T^{-1} e^{-D/T}$ for $T \ll D$), suggesting the Ni–Ni interactions play an important role at low temperatures (see more in section 3F). The d value obtained from the low temperature fit is very close to the T^3 dependence expected for 3D AFM spin waves.^{60,61} Hence, it is possible that **1** goes through a transition to LRO within the experimental temperature range. The lack of a λ peak is indicative of the presence of significant spatial exchange anisotropy among the magnetic interactions in **1**. In comparing the data for **1** and **2**, we predict Q2D magnetism for **1** with $J_{\text{pyz}} \gg J_{\perp}$ (for further

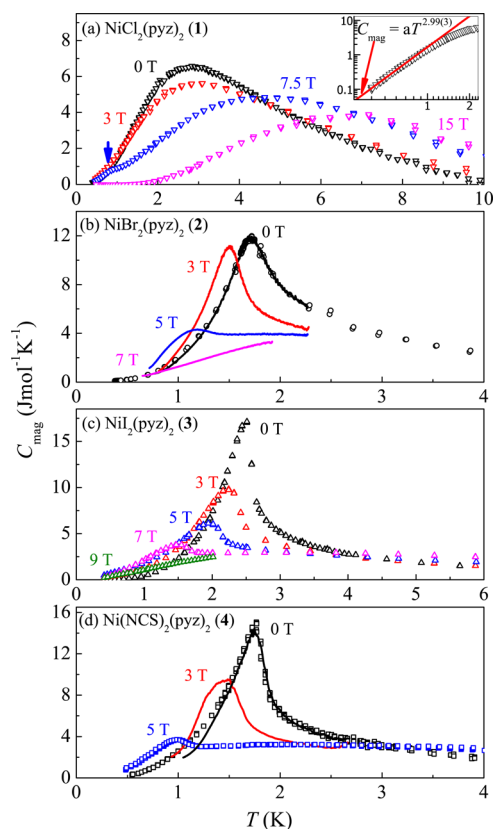


Figure 5. C_{mag} versus T for $\text{NiX}_2(\text{pyz})_2$ ($X = \text{Cl}$ (1), Br (2), I (3), and NCS (4)) under various magnetic fields. The open symbols and solid curves correspond to the data obtained by the traditional relaxation and dual-slope methods, respectively. Inset to a: the low-temperature section of the zero-field C_{mag} for 1 plotted on a logarithmic scale. The red line is a fit to the spin-wave expansion, $C_{\text{mag}} = aT^{d/n}$, for the $T < 0.6$ K data.

details, see section 4), where J_{pyz} and J_{\perp} are intra- and interlayer interactions, respectively. For a layered Heisenberg $S = 1$ antiferromagnet, the λ anomaly diminishes and becomes nearly quenched when $J_{\perp}/J_{\text{pyz}} = 0.01$.⁶² In the case of 1, the J_{\perp}/J_{pyz} ratio at which the λ anomaly vanishes is expected to deviate from 0.01 due to the presence of D , which may reduce the degrees of freedom of the $\text{Ni}(\text{II})$ spins. Nevertheless, we expect J_{\perp} to be at least an order of magnitude smaller than J_{pyz} ($J_{\perp}/J_{\text{pyz}} < 0.1$) in order to explain the absence of a λ anomaly in 1.

Figure 5 shows the temperature dependence of C_{mag} at various magnetic fields. For 1, a small shoulder develops below 2 K upon the application of a magnetic field up to 7.5 T (indicated by the arrow). Above 7.5 T, the broad peak for 1 moves to higher temperatures, which is due to the Zeeman splitting effect on the magnetic band structure. The field dependences of C_p for 2–4 are similar to each other and the LRO temperature is suppressed by application of a magnetic field. The phase diagrams for 2–4 are shown in Figure 6. The open symbols and solid squares are the phase boundary extracted by $C_p(T)$ and MCE, respectively. The phase boundaries observed in 2 and 4 are commonly seen in the phase diagram of a 3D antiferromagnet. The amplitude of the specific-heat anomalies at zero-field diminish from 17 J/(K·mol) (3) to 12 J/(K·mol) (2). In particular, 2 and 4 exhibit the same LRO temperature whereas the height of the λ -peak is reduced from 15 J/(K·mol) (4) to 12 J/(K·mol) (2). The reduction in the amplitude of the λ peak is often indicative of a diminishing interlayer interaction.³⁹

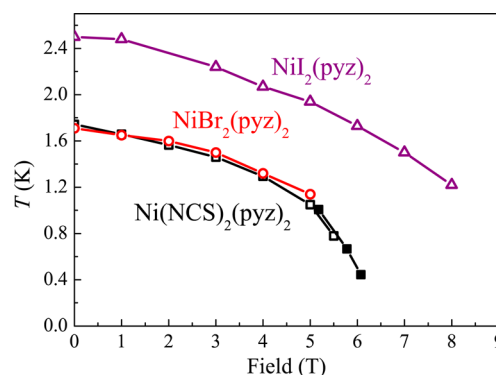


Figure 6. Phase boundary for 2 (○), 3 (△), and 4 (□ and ■) measured by heat capacity and MCE. The open symbols and the solid squares are extracted by heat capacity and MCE, respectively.

C. Search for Long-Range Magnetic Order Using μSR .

Example μSR spectra measured on $\text{NiBr}_2(\text{pyz})_2$ (2) using the GPS at the Swiss Muon Source are shown in Figure 7. Across the

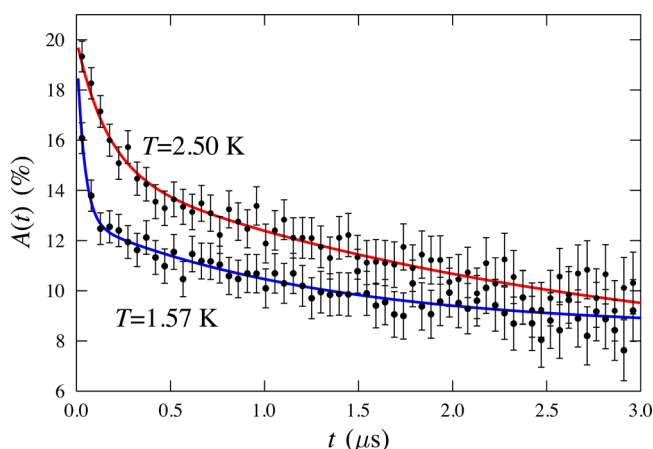


Figure 7. Example ZF $\mu^+\text{SR}$ data measured on $\text{NiBr}_2(\text{pyz})_2$ (2) above and below the transition at 1.9(1) K. The solid lines are fits of the data to eq 3.

measured temperature range $1.5 \leq T \leq 5$ K, we observed monotonic relaxation with no resolvable oscillations in the spectra. (In fact, we found that the spectra for materials 1–3 all share the same form.) The spectra were found to be well described by the function

$$A(t) = A_1 e^{-\lambda_1 t} + A_2 e^{-\lambda_2 t} + A_{\text{bg}} \quad (3)$$

where the initial amplitude $A(0)$ was held fixed. A_1 and A_2 correspond to the fast and slow relaxing components, respectively. The temperature evolution of the fitted parameters for 2 is shown in Figure 8c and d. In both the spectra (Figure 7) and in the behavior of the fitted parameters (Figure 8c and d), we see a sharp discontinuity on cooling through $T \approx 1.9$ K. This involves a decrease in the amplitude A_2 of the slowly relaxing component with relaxation rate λ_2 , implying an increase in the amplitude A_1 of the component with relaxation rate λ_1 . The fact that the nonrelaxing component A_{bg} increases sharply implies a transition to a regime with a static distribution of local fields in the sample. This is because those muons whose spins lie parallel to the static local magnetic field at the muon site will not be relaxed²⁶ and will therefore contribute to the nonrelaxing amplitude A_{bg} . In addition, the relaxation rates would be

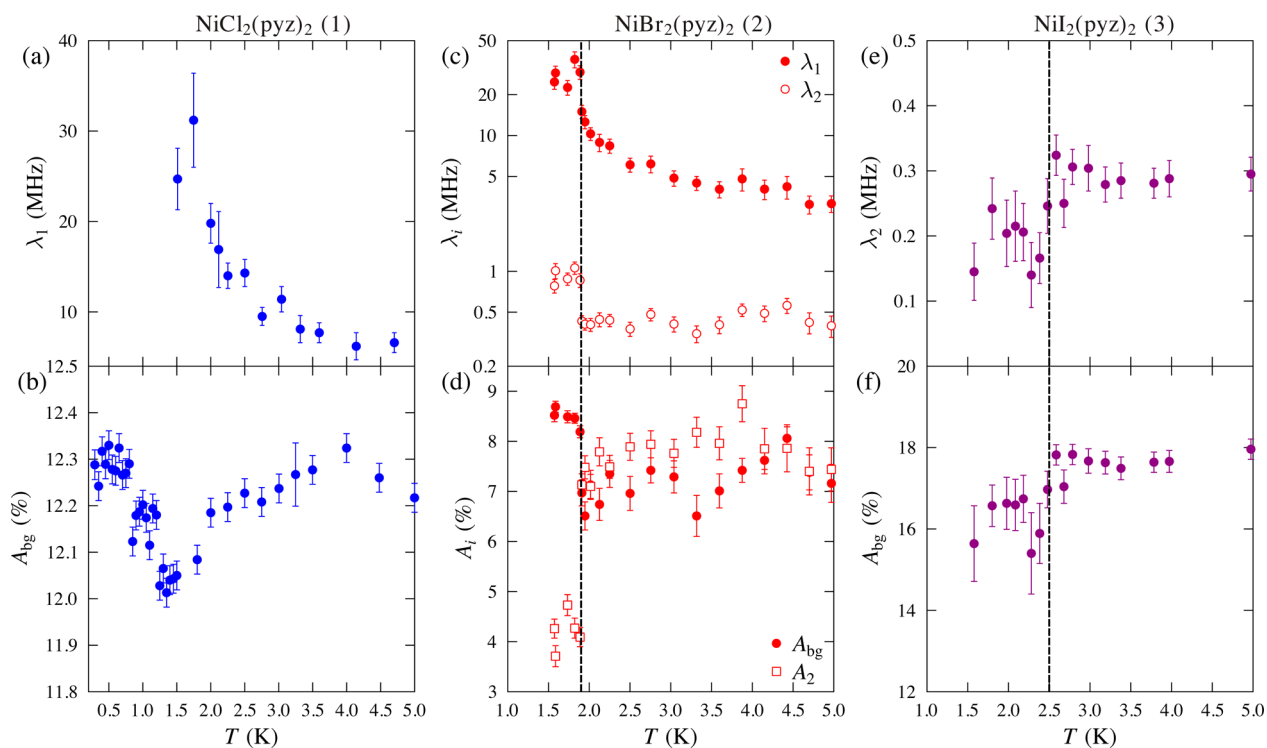


Figure 8. Temperature evolution of selected parameters in eq 3 for materials 1 (a and b), 2 (c and d), and 3 (e and f). Plot b shows that a broad minimum is observed in the nonrelaxing component (A_{bg}) for 1 around 1.5 K. Sharp discontinuities are observed in the fitted parameters for 2 and 3 (plots c–f) at 1.9 and 2.5 K, respectively, indicating a magnetic transition at these temperatures. The vertical dash lines are guides for the eyes showing the temperatures at which magnetic ordering occurs in 2 and 3.

expected to be proportional to the second moment of the local magnetic field distribution (B^2). The rapid increase in relaxation rates λ_1 and λ_2 therefore probably implies an increase in the magnitude of the local magnetic fields at the muon sites. Taken together, these phenomena point toward a transition to a regime of magnetic order taking place at $T_N = 1.9(1)$ K in 2, which is in reasonable agreement with the peak observed in C_p .

Measurements on $\text{NiI}_2(\text{pyz})_2$ (3) were made using the MuSR spectrometer at ISIS. The pulsed muon beam at ISIS has a time width $\tau \approx 80$ ns, which limits the time resolution to below $\sim 1/\tau$. As a result, we were unable to resolve the fast relaxation (with rate λ_1) that we considered in the data for material 2, which manifests itself as missing asymmetry. Instead, we plot the slow relaxation rate (Figure 8e) and the baseline asymmetry (A_{bg} ; Figure 8f), which show discontinuities upon magnetic ordering around a temperature $T_N = 2.5(1)$ K, in agreement with the anomaly in the heat capacity.

Measurements were made on $\text{Ni}(\text{NCS})_2(\text{pyz})_2$ (4) using the ARGUS spectrometer at the ISIS facility. In this case, the spectra showed weak exponential relaxation in the regime $0.35 \leq T \leq 4$ K with no discontinuities observed that would reflect the ordering temperature seen in the heat capacity at $T_N = 1.8$ K. It is unclear why the muon should be insensitive to the ordering transition in this material, although we note the possibility of the muon forming bound states with the electronegative NCS^- and therefore being insensitive to the ordering of the electronic moments. However, this was not the case in $\text{Fe}(\text{NCS})_2(\text{pyz})_2$,⁶³ where the spectra were of the same form as observed for materials 1–3 where and the magnetic ordering transition was observed.

For measurements made on $\text{NiCl}_2(\text{pyz})_2$ (1) using the GPS spectrometer, no sharp change in the form of the spectra is observed in the accessible temperature range $T > 1.5$ K, although

we saw a steep rise in the fast relaxation rate (Figure 8a) as temperature was lowered below 2 K. In order to search for magnetic order in 1, measurements were made down to 0.35 K using a sorption cryostat with the EMU spectrometer at ISIS. As in the case of 1, the ISIS resolution limit prevented us from resolving fast relaxation in this case. Instead, it was instructive to follow A_{bg} as a function of temperature, shown in Figure 8b. On cooling, we see a sharp decrease below 2 K, leading to a minimum in asymmetry centered around 1.5 K. The decrease in asymmetry on cooling is probably due to the increase in relaxation of the muon spins. This is followed by an increase at lower temperatures probably reflecting a regime where the moments are more static. It is possible that this minimum reflects a magnetic transition in material 1, although the difference in the heat capacity for this compound compared to others in the series means that this is unlikely to be a transition to a regime of long-range magnetic order. Instead, it is possible that the changes in the μSR spectra we observe in the 1.5–2 K region reflect a freezing-out of dynamic relaxation channels causing moments to become more static on the muon (μs) time-scale.

D. Electron Spin Resonance. Electron spin resonance (ESR) measurements were performed on powder samples of 1–4 to probe the ZFS and the g factor associated with $\text{Ni}(\text{II})$ ions. A thorough search for ESR absorption in $\text{NiCl}_2(\text{pyz})_2$ (1) at 130 GHz gave no indication for any ESR signal in the temperature range $1.9 \leq T \leq 300$ K, in contrast to 2–4. The lack of ESR signal in 1 is indicative of the presence of a sizable ZFS ($|D| \geq 6.24$ K) for 1. The representative ESR spectra for $\text{NiBr}_2(\text{pyz})_2$ (2) and $\text{Ni}(\text{NCS})_2(\text{pyz})_2$ (4) at 50 K are shown in Figure 9 and were recorded in the first-derivative mode. A single ESR transition was observed for 2 and 4 up to 6 T. The broad ESR line-width for 2 is likely due to a structural-disorder-induced

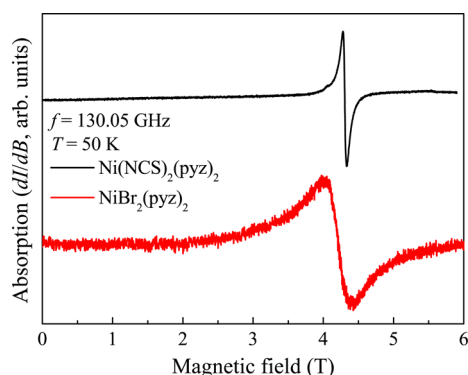


Figure 9. Representative 130 GHz ESR spectra for **2** (red) and **4** (black) collected at 50 K. The absorption ESR spectra are recorded in the first derivative mode.

g-strain/ D -strain^{64,65} as shown by crystallography data. In the high temperature regime ($T \gg T_N$), the observed ESR signal corresponds to single-spin excitations associated with Ni(II). For $S = 1$ Ni(II) with a nonzero ZFS and/or anisotropic g factor, a powder ESR spectrum is expected to show multiple transitions which correspond to the field being parallel/perpendicular to the magnetic-principle axis of the Ni(II) site. The observation of a single transition in ESR spectra suggests that $D = 0$ as well as $g_x = g_y = g_z$ for Ni(II) ions in **2** and **4**. The center of the transition gives $g = 2.20(5)$ and $g = 2.16(1)$ for **2** and **4**, respectively. The ESR spectra for $\text{NiI}_2(\text{pyz})_2$ (**3**) recorded at 130 GHz (not shown) only exhibit an extremely broad feature which is not applicable for a quantitative analysis.

Further variable frequency/temperature ESR measurements were performed on **2–4** in a broadband ESR spectrometer. Representative ESR spectra are shown in Figure 10. The spectra

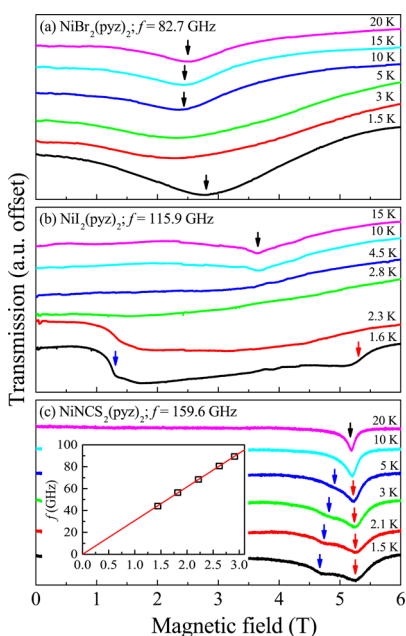


Figure 10. Temperature dependence of the ESR spectra for powder samples of (a) $\text{NiBr}_2(\text{pyz})_2$ (**2**), (b) $\text{NiI}_2(\text{pyz})_2$ (**3**), and (c) $\text{Ni}(\text{NCS})_2(\text{pyz})_2$ (**4**) recorded at 82.7, 115.9, and 159.6 GHz, respectively. The spectra are recorded in the transmission mode. The inset to c shows the frequency versus field plot for the ESR resonance observed in **4** at 50 K. The solid line corresponds to a fit of the data with $g = 2.18(3)$ and $D = 0$.

were recorded in the transmission mode. The 20 K spectra for **2** and **4** (Figure 10a and c) are consistent with the aforementioned 130 GHz results where a single transition was observed, suggesting $D = 0$ and $g_x = g_y = g_z$. Additional multifrequency ESR measurements were performed on **4** to confirm the absence of D in the compound (inset to Figure 10c). The 15 K spectrum for **3** (Figure 10b) exhibits a broad feature which spreads over the entire field range (6 T). This feature is reminiscent of a spectrum for $g = 2.27(8)$ and $D = 0$ Ni(II) ions. The broad line width associated with the ESR signal of **3** is likely due to g -strain/ D -strain and/or the presence of non-Heisenberg interactions⁶⁶ between Ni(II) ions (see below).

Upon cooling, the ESR resonance fields and line-widths for **2–4** show substantial variations as the temperature approaches the onset of LRO. The temperature-dependence of the spectra above T_N may be attributed to short-range spin correlations.^{67,68} When the temperature approaches T_N , it is conceivable that small clusters of spins can be strongly correlated and exhibit properties that prefigure the long-range ordered behavior. At low temperatures, the spectra for **2–4** show distinct differences. For **2**, a single resonance was observed down to base temperature. On the other hand, two resonances were observed in the low temperature spectra for **3** and **4**, as indicated by the blue and red arrows in Figure 10b and c. It is known that ESR probes antiferromagnetic resonances when $T < T_N$ where the multiple resonances correspond to the applied field being parallel/perpendicular to the collective anisotropy field and/or different AFM modes in powder samples.⁶⁹ In either case, the observation of multiple ESR transitions in the low temperature spectra for **3** and **4** reveals the presence of a collective anisotropy field in these two compounds. Due to the fact that no single-ion ZFS was found for **3** and **4** at high temperatures, the collective anisotropy fields are likely due to non-Heisenberg interactions between Ni(II) ions. By contrast, the anisotropy field in **2** is likely to be negligible as only a single transition is observed down to the lowest temperature.

Quantitative calculations of the anisotropy fields in **3** and **4** are complicated by the fact that the transition temperatures are significantly affected by the applied field (see the phase diagram in Figure 6). In the experimental temperature regime, most low temperature spectra spread across the phase boundary, which makes it very difficult to simulate the ESR spectra with any standard model. Qualitatively speaking, the spacing between the two resonances in **3** is almost 4 times of that of **4**, suggesting the presence of a stronger anisotropy field in **3** than **4**. This is confirmed by the spin-flop transition observed in these two compounds (see below).

E. Pulsed Field Magnetization. Magnetization versus field data (M vs H) were recorded between 0.45 and 10 K using pulsed-magnetic fields up to 60 T and are shown in Figure 11a. At low temperatures, all compounds exhibit a slow initial rise in M , which gradually increases in slope until the critical field (H_c) is approached. $\mu_0 H_c = 6.9(6)$, $6.1(3)$, and $5.8(1)$ T for $\text{NiCl}_2(\text{pyz})_2$ (**1**), $\text{NiBr}_2(\text{pyz})_2$ (**2**), and $\text{Ni}(\text{NCS})_2(\text{pyz})_2$ (**4**), respectively, as defined by the midpoint between the peak in dM/dH (indicated by * in the inset to Figure 11) and the region where dM/dH remains essentially constant (inset to Figure 11). The slight concavity of the M vs H curve is expected for antiferromagnetic $S = 1$.⁷⁰ In the case of $\text{NiI}_2(\text{pyz})_2$ (**3**), the dM/dH curve exhibits extra steps between 6 and 10 T, which may be attributed to non-Heisenberg exchange interactions as well as the polycrystalline nature of the sample. The presence of non-Heisenberg interactions can give rise to an anisotropic critical

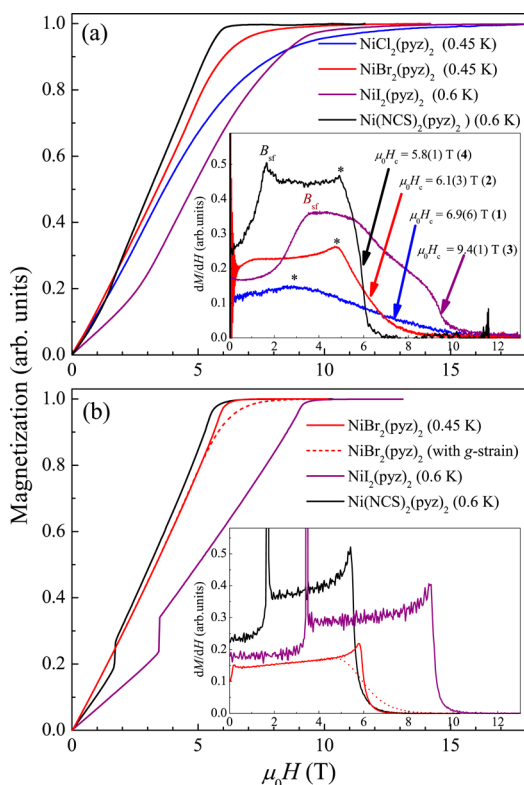


Figure 11. (a) Main plot: Isothermal magnetization for $\text{NiCl}_2(\text{pyz})_2$ (1), $\text{NiBr}_2(\text{pyz})_2$ (2), $\text{NiI}_2(\text{pyz})_2$ (3), and $\text{Ni}(\text{NCS})_2(\text{pyz})_2$ (4) acquired well below their ordering temperatures for 2–4. Inset: dM/dH plot showing the spin-flop transition (B_{sf}) and critical fields (B_c). (b) Main plot: Calculated magnetization M for $\text{NiBr}_2(\text{pyz})_2$ (red), $\text{NiI}_2(\text{pyz})_2$ (purple), and $\text{Ni}(\text{NCS})_2(\text{pyz})_2$ (black) employing an $S = 1$ square lattice with interlayer interactions (eq 4). Inset: dM/dH plot for the calculated magnetization. The dashed lines in both the main plot and the inset represent the simulation for $\text{NiBr}_2(\text{pyz})_2$ including a broadening effect induced by g -strain.

field, leading to extra steps at high fields in the dM/dH curve of a powder sample. The critical field for 3 is defined by the midpoint between the last kink in dM/dH and the region where dM/dH drops to zero. It is noteworthy that due to the possibility of an anisotropic critical field, this assigned value [9.4(1) T] for 3 may be an overestimation and actually correspond to the largest component of the anisotropic H_c .

For 3 and 4, low-field anomalies occur at 3.46 and 1.68 T, respectively, which are attributed to a field-induced spin-flop transition. It is well established^{71,72} that the spin-flop field $B_{\text{sf}} = \mu_0 H_{\text{sf}}$ is related to the anisotropy field H_A and the exchange field H_E ($\approx H_c/2$) by $H_{\text{sf}}^2 = 2H_E H_A - H_A^2$. Based on this relation, the anisotropy fields are estimated to be 1.52 and 0.54 T for 3 and 4,

respectively. No evidence of a spin-flop transition was found for 1 and 2. The magnetization data for 2–4 are consistent with the low-temperature ESR spectra; i.e., the anisotropy field of 2 is negligible, whereas that of 3 was found to be significant. An intermediate anisotropy field was observed in 4.

The rounded nature of M in the vicinity of H_c could be due to several reasons, including the powdered nature of the samples, a sizable zero-field splitting, or anisotropic g factors. For 4, the gradient of the $M(H)$ curve decreases rapidly until M saturates at around 6 T. In comparison, the transitions from nearly linearly increasing to saturated behavior in the M vs H curves for 1 and 2 is broadened, as is often found in polycrystalline samples in several Ni(II)-based polymeric magnets. This difference in the transitions for 1, 2, and 4 is in line with the ESR results. The ESR spectra for 4 are indicative of the absence of ZFS as well as an isotropic g associated with Ni(II), leading to a sharp transition in the vicinity of H_c . Whereas in 1, the lack of ESR signal up to 130 GHz ($= 6.24$ K) indicates the presence of a sizable ZFS in Ni(II) ($|D| \geq 6.24$ K), which leads to an extremely broad transition in the magnetization curve. For 2, though $D = 0$ and g is isotropic, the broad ESR line width implies a broad distribution of g (g -strain), resulting in an intermediate broadened transition in its M versus H data.

Figure 11b shows the calculated magnetization for 2–4 at low T . The simulations are performed using the stochastic series expansion (SSE) method⁴⁴ employing the following Hamiltonian:

$$H = \sum_{\langle ij \rangle_y} J_{\text{pyz}} (S_i^x S_j^x + S_i^y S_j^y + \Delta S_i^z S_j^z) + \sum_{\langle ij \rangle_z} J_{\perp} (S_i^x S_j^x + S_i^y S_j^y + \Delta S_i^z S_j^z) - \sum_i \vec{B} \cdot \vec{S}_i \quad (4)$$

The simulations were performed with $J_{\text{pyz}} = 1.00$ K and $J_{\perp} = 0.26$ K for 2, $J_{\text{pyz}} = 0.85$ K and $J_{\perp} = 1.34$ K for 3, and $J_{\text{pyz}} = 0.74$ K and $J_{\perp} = 0.42$ K for 4. In the simulations, the ratio between J_{pyz} and J_{\perp} was fixed according to the magnetic dimensionality analysis (see section 4 and Table 3), while their values have been slightly fine-tuned to match the experimental data. Additionally, we allowed an Ising-like interaction with $\Delta = 1.35$ and 1.20 for 3 and 4, respectively, to account for the low-field spin-flop transition. $\Delta = 1$ (Heisenberg interaction) for 2 as no collective anisotropy was observed. In the simulations, we obtained the powder averages by calculating the magnetization curves M_x for $\vec{B} = B\hat{x}$ and M_z for $\vec{B} = B\hat{z}$ then using the mean field relation $M_p = \frac{1}{3}M_z + \frac{2}{3}M_x$. In the calculation, we neglected the demagnetizing field and assumed $B = \mu_0 H$.

As shown in Figure 11, good agreement between the experiments and simulations was obtained for 2 and 4. For 2, the rounded feature of M in the vicinity of H_c could be reproduced by

Table 3. Magnetochemical Parameters Obtained for 1–4^a

	J_{pyz} (K)	J_{\perp} (K)	D (K)	g [$\chi(T)$]	g (ESR)	T_N (K)	$\mu_0 H_c$ (T)
$\text{NiCl}_2(\text{pyz})_2$ (1)	0.49 ± 0.01	< 0.05	8.03 ± 0.16	2.15 ± 0.05	n/a	n/a	6.9 ± 0.6
$\text{NiBr}_2(\text{pyz})_2$ (2)	1.00 ± 0.05	0.26 ± 0.05	0	2.10 ± 0.09	2.20 ± 0.05	1.8 ± 0.1	6.1 ± 0.3
$\text{NiI}_2(\text{pyz})_2$ (3)	< 1.19	> 1.19	0	2.41 ± 0.03	2.27 ± 0.08	2.5 ± 0.1	9.4 ± 0.1
$\text{Ni}(\text{NCS})_2(\text{pyz})_2$ (4)	0.82 ± 0.05	0.47 ± 0.05	0	2.10 ± 0.04	2.16 ± 0.01	1.8 ± 0.1	5.8 ± 0.1

^aThe J_{pyz} , D , and g for $\text{NiCl}_2(\text{pyz})_2$ (1) were obtained by fitting the DC susceptibility to an anisotropic 2D model, while its J_{\perp} was estimated based on the heat capacity data (see section 3B). The g values obtained via ESR data and through fitting of $\chi(T)$ are both listed in the table for comparison. The parameters for $\text{NiBr}_2(\text{pyz})_2$ (2), $\text{NiI}_2(\text{pyz})_2$ (3), and $\text{Ni}(\text{NCS})_2(\text{pyz})_2$ (4) were determined by analysis of the heat capacity, ESR, and pulsed magnetic field data (see section 4).

including a disorder induced g strain which leads to a Gaussian distribution of the g factor. The inclusion of the Ising-like interactions ($\Delta > 1$) leads to a spin-flop transition in **3** and **4**, as shown by the anomaly in dM/dH . However, the simulation for **3** does not show any obvious kink at high fields in dM/dH with Δ alone. The Ising-like interactions in **3** give rise to a 0.2 T difference between the critical fields with $B \parallel z$ and $B \perp z$, which appears to be insufficient to explain the high-field feature in experiments, suggesting additional anisotropy terms are needed to explain the magnetization data for **3**.

Further investigations are required to fully understand the spin-flop transition in **3** and **4**. The anisotropic part of the interaction, $J(\Delta - 1)$, should be proportional to $(\Delta g/g)^2$,⁷³ where Δg is the g anisotropy of Ni(II). Therefore, it seems to be contradictory to the J action, whereas no g anisotropy was observed in the ESR data. We suspect that the single-ion anisotropy of Ni(II) is not fully resolved due to non-Heisenberg interactions which broaden the ESR spectra.⁶⁶ Further experiments have been proposed on their magnetically diluted congeners, $\text{Zn}_{1-x}\text{Ni}_x\text{X}_2(\text{pyz})_2$ ($x \ll 1$), to investigate the Ni(II) anisotropy.

F. Magnetic Susceptibility and Density-Functional Theory (DFT). DC susceptibility measurements have been previously reported for **1** and **2**. The data were fitted to an anisotropic 2D model which gave $D = 7.92$ and 14.8 K, $zJ = 0.39$ and 0.95 K ($z = 4$), and $g = 2.17$ and 2.31 for **1** and **2**, respectively.^{32,33} Having discussed the magnetic dimensionality and the single-spin anisotropy from the aforementioned measurements, we now remeasure/analyze the DC susceptibility data for **1** and **2** (see Figure 12a and b). Upon cooling from

of AFM interactions in **1–4**. The fitted g values for **2** and **4** are in good agreement with the ESR results. The fitted g value for **3** deviates from the ESR result ($g = 2.27$) and appears to be too large for Ni(II). It is well-known that the g factor obtained from susceptibility can be affected by many experimental parameters, e.g., errors in the sample mass, whereas ESR gives a direct measurement for the g factor. Therefore, for **2–4**, the g factors extrapolated from the ESR data were used in the following data analysis.

Based on the information obtained from the heat capacity and ESR studies, the $\chi(T)$ data for **2–4** were fitted to an $S = 1$ simple cubic Heisenberg model, $\hat{H} = J \sum \langle i, j \rangle \hat{S}_i \cdot \hat{S}_j$. This model assumes that (a) the intra-/interlayer interactions are the same ($=J$) and (b) the number of nearest magnetic neighbors, z , is 6, both of which may be oversimplifications. As we will mention in the Discussion section, this model cannot account for the ordering temperature. Nevertheless, we can still use it to compare zJ with the pulsed field magnetization data. Figure 12 shows the data and fits for **2–4** over the entire temperature range with the fitting parameters of $J = 0.82(5)$ K (**2**), $J = 1.00(4)$ K (**3**), and $J = 0.75(2)$ K (**4**). These interactions would predict critical fields of $\mu_0 H_c = 6.66$, 8.4 , and 6.2 T for **2**, **3**, and **4** ($g = 2.20$ (**2**), $g = 2.27$ (**3**), and 2.16 (**4**) from the ESR data), respectively. The estimated critical fields for **2** and **4** are in excellent agreement with the pulsed field data. The estimated critical field for **3** is slightly less than that measured in the magnetization data. However, as we mentioned in the previous section, the possibility of an anisotropic H_c may lead to an overestimation in the magnetization data, which could account for this difference.

The susceptibility for **1** was fitted employing an anisotropic 2D model (Figure 12a).⁷⁴ The fit gives $zJ_{\text{pyz}} = 1.97(4)$ K, $D = 8.03(16)$ K, and $g = 2.15(5)$. Taking $z = 4$ (for Q2D model), $J_{\text{pyz}} = 0.49(1)$ K, which is almost half of that in **2–4**. The fitted easy-plane type anisotropy $D = 8.03$ K gives rise to a broad peak (Schottky anomaly) around 3 K which coincides with the broad feature in C_p for **1**. However, extracting D and J simultaneously from powder magnetic data can often be unreliable as the two parameters are highly correlated. The result is not unique and varies dramatically depending on the model employed in the analysis. In fact, the susceptibility data for **1** can be fitted with an isolated $S = 1$ model with $D = 13.3$ K. However, this would predict a broad peak around 5 K in the zero-field heat capacity, which significantly deviates from the experimental results. Therefore, both D and J are required for characterizing **1**. Because single crystals for **1** are currently unavailable, it is not possible to distinguish between the parallel and perpendicular susceptibilities in order to uniquely determine the sign and magnitude of D .

As an additional evaluation of the magnetic interactions, density functional theory (DFT) calculations were performed using the aforementioned structural data for **1–4**. The magnetic interactions through the pyz bridges were modeled by the dinuclear fragments, $(\text{pyz})_3\text{NiX}_2(\mu\text{-pyz})\text{NiX}_2(\text{pyz})_3$, consisting of two $(\text{pyz})_3\text{NiX}_2$ segments connected by a bridging pyz ligand ($\mu\text{-pyz}$), which mediates the intralayer interaction J_{pyz} . The calculations give weak AFM interactions mediated by Ni–pyz–Ni bonds throughout all compounds as expected. J_{pyz} is calculated to be 1.85, 2.41, and 3.16 K for compounds **1**, **2**, and **3**, respectively. Separate DFT calculations were performed for **4** due to its lower symmetry ($C2/m$ vs $I4/mmm$ for **1–3**). In general, the adjoining orthogonal pyz bridges in **4** afford different magnetic interactions depending on whether the Ni–Ni linkage lies in or perpendicular to the Ni–NCS planes. Therefore, DFT

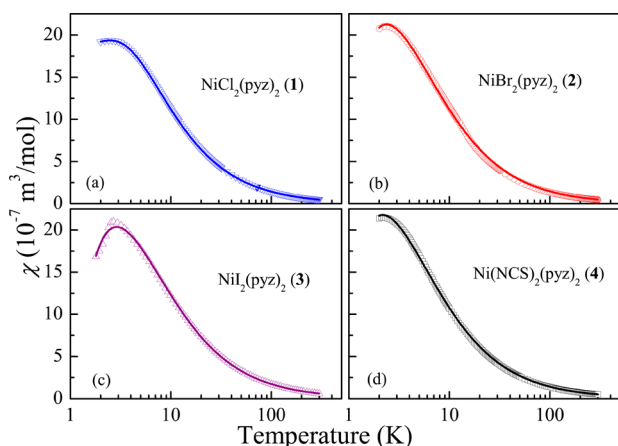


Figure 12. Magnetic susceptibility data for powder sample of **1** (a), **2** (b), **3** (c), and **4** (d) collected with an applied magnetic field of $\mu_0 H = 0.1$ T. The solid lines represent fits of χ vs T (see detailed discussion in the main text).

300 K, $\chi(T)$ increases smoothly, reaching a broad maximum near 2.6, 2.4, 2.7, and 2.2 K for **1**, **2**, **3**, and **4**, respectively, and then drops slightly as the temperature is lowered to 2 K. This behavior can be caused by concomitant antiferromagnetic (AFM) coupling between $S = 1$ Ni(II) sites and/or ZFS of the spin ground state. Curie–Weiss fits of the reciprocal susceptibility in the temperature range of $50 < T < 300$ K lead to $g = 2.17(7)$ and $\theta = -3.51(23)$ K (**1**), $g = 2.10(9)$ and $\theta = -3.20(36)$ K (**2**), $g = 2.41(3)$ and $\theta = -5.02(6)$ K (**3**), and $g = 2.10(4)$ and $\theta = -4.00(23)$ K (**4**). In the absence of single-ion anisotropy, the negative Curie–Weiss temperatures would indicate the presence

calculations for **4** were performed with both configurations to investigate the influence of the NCS ligand orientation onto J_{pyz} . A small difference in J_{pyz} was found for these two configurations with J_{pyz} calculated to be 1.65 and 1.71 K for the Ni–Ni axis in and perpendicular to the Ni–NCS planes, respectively. The calculation for **4** suggests that J_{pyz} is almost independent of the orientation of the NCS ligands; hence, it is reasonable to treat the $[\text{Ni}(\text{pyz})_2]^{2+}$ layers in **4** as ideal magnetic square lattices in the data analysis.

4. DISCUSSION

Each of the four compounds share similar extended polymeric structures consisting of 2D square $[\text{Ni}(\text{pyz})_2]^{2+}$ sheets in the *ab* plane with the *X* ligands acting as spacers between layers. The Ni–Ni separations are similar along the Ni–pyz–Ni bridges. There is little variation of the closest interlayer Ni–Ni distance across all four compounds (7.32 Å for $\text{NiCl}_2(\text{pyz})_2$ (**1**), 7.54 Å for $\text{NiBr}_2(\text{pyz})_2$ (**2**), 7.90 Å for $\text{NiI}_2(\text{pyz})_2$ (**3**), and 7.23 Å for $\text{Ni}(\text{NCS})_2(\text{pyz})_2$ (**4**)). The difference in the magnetism of **1–4** clearly highlights that the selection of the *X* ligand can lead to significant changes in both the single-ion anisotropy and the magnetic dimensionality in this $\text{NiX}_2(\text{pyz})_2$ family.

Thorough investigations have been performed to quantify the magnetic interaction through *X*-bridges in $\text{CuX}_2(\text{pyz})$ compounds (*X* = F, Cl, Br and NCS).^{57,75–77} The $\text{CuX}_2(\text{pyz})$ compounds possess 2D rectangular lattices which are characterized by Cu–pyz–Cu chains linked by Cu–*X*–Cu bridges. We briefly review the interactions through the Cu–*X*–Cu bridges since they are likely related to the interlayer interactions through the *X* ligands in compounds **1–4**. In $\text{CuX}_2(\text{pyz})$ compounds, the AFM interactions through Cu–*X*–Cu bonds were found in the descending order of magnitude: Br > Cl > F > NCS. In particular, $\text{Cu}(\text{NCS})_2(\text{pyz})$ presents itself as a nearly ideal Q1D AFM chain with the primary 1D interactions mediated through the Cu–pyz–Cu bridges. μSR measurements for $\text{Cu}(\text{NCS})_2(\text{pyz})$ show no evidence for LRO above 0.35 K, which is indicative of extremely weak interchain interactions (<0.13 K) through the Cu–(NCS)₂–Cu bonds.⁷⁷ Therefore, it is at first glance surprising to see that $\text{Ni}(\text{NCS})_2(\text{pyz})_2$ (**4**) shows a strong λ anomaly as the interlayer interactions via the NCS[−] ligands are expected to be small. On the other hand, the difference between $\text{NiCl}_2(\text{pyz})_2$ (**1**) and $\text{NiBr}_2(\text{pyz})_2$ (**2**) may be explained by the previous studies with the less efficient Cl pathways leading to Q2D magnetism in **1**. The results for $\text{NiI}_2(\text{pyz})_2$ (**3**) are in line with this hypothesis that the larger I[−] ions can form more effective exchange pathways between $[\text{Ni}(\text{pyz})_2]^{2+}$ layers, leading to stronger interlayer interactions. Consequently, a larger λ -anomaly and a higher B_c are observed in the C_p and the magnetization data.

A similar λ -anomaly in C_p was observed in a compound isomorphous to **4**, $\text{Fe}(\text{NCS})_2(\text{pyz})_2$, which is regarded as an Ising Q2D antiferromagnet.⁷⁸ In $\text{Fe}(\text{NCS})_2(\text{pyz})_2$, although long-range order is achieved below 6.8 K, its critical parameters are ideally close to those expected for Q2D Ising systems. In the case of **2**, the scenario for an Ising Q2D antiferromagnet is excluded due to the facts that (a) the ZFS of the Ni(II) ions in **2** is found to be negligible and (b) both the ESR and magnetization data show no evidence of a collective anisotropic field at low temperatures. For **3** and **4**, the absence of single-ion anisotropy in their paramagnetic phase is also unfavorable of extreme Ising Q2D antiferromagnets. In particular, the phase boundary of **4** is similar to that of 3D antiferromagnets, providing additional support for 3D antiferromagnetism in **4**. Therefore, it is most likely that

the *X*[−] ligands serve as bridging ligands in **2–4**, which mediate interlayer interactions that are comparable to the intralayer interactions, leading to AFM long-range order. The difference between the NCS[−] bridges in $\text{Cu}(\text{NCS})_2(\text{pyz})$ and **4** remain to be examined. The shortest Ni–S distance in **4** is 4.719 Å, which is unlikely to form a direct Ni–S exchange pathway. Therefore, the interlayer interactions in **4** may be mediated through overlapping electron density among NCS[−] ligands connected to Ni(II) ions belonging to adjacent layers.

In discussing the susceptibility for **1–4**, a simple cubic model was employed for the data analysis. However, the legitimacy of using such a model needs to be justified. It is clear that each Ni(II) ion has four magnetic neighbors in its $[\text{Ni}(\text{pyz})_2]^{2+}$ plane for all four compounds. However, it is not straightforward to tell the number of magnetic neighbors in the adjacent planes from the crystal structures. For **1–3**, each Ni(II) ion has eight equally spaced neighbors in the adjacent planes. In the case of perfect tetragonal symmetry, this gives eight equivalent magnetic neighbors in the adjacent planes for a Ni(II) site, leading to frustration of the minimum-energy configuration if the interactions within the $[\text{Ni}(\text{pyz})_2]^{2+}$ planes are antiferromagnetic.⁷⁹ In with this case, **1–3** would only show two-dimensional order within the $[\text{Ni}(\text{pyz})_2]^{2+}$ planes, and the λ -anomaly would be significantly suppressed, contrary to the experimental observations. Therefore, we speculate that the frustration is relieved via breaking of the tetragonal symmetry, possibly due to the structural disorder of the pyz rings, resulting in 3D LRO in **2** and **3**. A reduced symmetry should give rise to four inequivalent interlayer interactions in **1–3** with one of them being stronger than the others. Compound **4** crystallizes in a monoclinic space group where one would expect four inequivalent interlayer interactions based on its structure. Therefore, it is reasonable to assume that the interlayer interactions are dominated by one particular pathway in **1–4**, and each Ni(II) ion has two magnetic neighbors in the adjacent planes (one in the plane above/below). Although this is probably an oversimplification, it is the simplest model one can adopt is consistent with the experimental results.

The critical fields measured in the pulsed magnetic field data provide a reliable way to probe the interactions between Ni(II). Here, we focus on **2–4**, for which no single-ion ZFS was observed by ESR. Consequently, $B_c = \mu_0 H_c$ solely depends on the intra- and interlayer interactions. The critical field for **1** depends on both *D* and *J*, and it is not possible to deconvolute them from pulsed field data alone. For quantitative calculation of the intra-/interlayer interactions, the critical fields and the Néel temperatures for **2–4** are analyzed within a Q2D Heisenberg model. For *S* = 1 Q2D Heisenberg antiferromagnets, the critical field is

$$\mu_B g B_c = 8J_{\text{pyz}} + 4J_{\perp} \quad (5)$$

where J_{\perp} is the interlayer interaction. Yasuda et al. proposed an empirical correlation⁸⁰ between T_N and the interactions based on quantum Monte Carlo calculations for *S* = 1 Q2D Heisenberg antiferromagnets:

$$T_N = 4\pi \times 0.68 J_{\text{pyz}} / [3.12 - \ln(J_{\perp}/J_{\text{pyz}})] \quad (6)$$

Equation 6 is valid in the range $0.001 \leq J_{\perp}/J_{\text{pyz}} \leq 1$. In the analysis, we assumed $\Delta = 1$ due to the lack of theoretical study to correlate Δ and T_N in *S* = 1 antiferromagnets. Applying eq 5 and eq 6 to **2–4**, it is found that the experimental results for **2** and **4** can be accounted for with the following parameter sets: $J_{\text{pyz}} = 1.0$ and $J_{\perp} = 0.26$ K for **2** and $J_{\text{pyz}} = 0.82$ and $J_{\perp} = 0.47$ K for **4**.

The obtained J_{pyz} 's are similar for **2** and **4**, which is consistent with the structural similarities between their $[\text{Ni}(\text{pyz})_2]^{2+}$ layers. $J_{\perp}/J_{\text{pyz}} = 0.26$ and 0.57 for **2** and **4**, respectively, indicating **2** is a 3D antiferromagnet which prefigures some Q2D magnetism, whereas **4** is more similar to an ideal 3D antiferromagnet in which the intra- and interlayer interactions are equivalent. The difference in J_{\perp}/J_{pyz} explains the reduction of the λ -anomaly in **2**. On the other hand, no J_{\perp} and J_{pyz} can satisfy eq 5 and eq 6 simultaneously for **3**, suggesting it does not fall into the category of a Q2D antiferromagnet. We suspect that the large Γ^- ligands form efficient exchange pathways which propagate strong interlayer interactions, leading to $J_{\perp} > J_{\text{pyz}}$ in **3**. Hence, its LRO temperature and critical field cannot be interpreted in terms of a Q2D antiferromagnet. Absence of an adequate theoretical model of for an $S = 1$ antiferromagnet with $J_{\perp} > J_{\text{pyz}}$ it is difficult to calculate J_{\perp} and J_{pyz} independently. In the case of an ideal 3D antiferromagnet, $J_{\perp} = J_{\text{pyz}} = 1.19$ K for **3**. With $J_{\perp} > J_{\text{pyz}}$ eq 5 suggests $J_{\text{pyz}} < 1.19$ K for **3**. However, among the four compounds, **3** exhibits the strongest λ anomaly, indicating that it is reasonably close to a 3D antiferromagnet. Accordingly, we expect J_{pyz} for **3** to be close to 1.19 K. The resulting parameters for **3** are $J_{\perp} = 1.19$ K and $J_{\text{pyz}} = 1.19$ K.

Finally, we compare the results of **1–4** with those of $[\text{Ni}(\text{HF}_2)(\text{pyz})_2]\text{Z}$ ($\text{Z} = \text{PF}_6^-$ and SbF_6^-). The 2D $[\text{Ni}(\text{pyz})_2]^{2+}$ layers found in **1–4** exhibit very similar geometrical parameters to those of $[\text{Ni}(\text{HF}_2)(\text{pyz})_2]\text{Z}$. The $[\text{Ni}(\text{HF}_2)(\text{pyz})_2]\text{Z}$ compounds were found to be quasi-1D magnets composed of Ni–FHF–Ni chains (J_{1D}) with interchain coupling (J_{\perp}) mediated by Ni–pyz–Ni linkages. The interaction parameters were not determined due to difficulties in distinguishing between J_{1D} , J_{\perp} , and D from pulsed-field data as above. The couplings through Ni–pyz–Ni in the vicinity of 1 K, which are significantly smaller than J_{1D} determined for $[\text{Ni}(\text{HF}_2)(\text{pyz})_2]\text{Z}$. Such results are consistent with the Q1D magnetism of $[\text{Ni}(\text{HF}_2)(\text{pyz})_2]\text{Z}$. Our study also shows that the selection of the axial X^- ligands can substantially vary the ZFS of the $\text{Ni}(\text{II})$ ion as well as potentially introduce non-Heisenberg interactions between $\text{Ni}(\text{II})$ ions, leading to different magnetic ground state structures in $\text{Ni}(\text{II})$ -based magnets.

5. SUMMARY

Four $\text{Ni}(\text{II})$ -based coordination polymers were prepared and their structures carefully examined. $\text{NiCl}_2(\text{pyz})_2$ (**1**), $\text{NiBr}_2(\text{pyz})_2$ (**2**), $\text{NiI}_2(\text{pyz})_2$ (**3**), and $\text{Ni}(\text{NCS})_2(\text{pyz})_2$ (**4**) feature 2D square $[\text{Ni}(\text{pyz})_2]^{2+}$ planes stacking along the c axis spaced by X ligands ($\text{X} = \text{Cl}, \text{Br}, \text{I}, \text{or NCS}$). Heat capacity measurements are indicative of the presence of long-range order for **2–4** and Q2D magnetism for **1** suggest that a transition occurs from 3D to 2D magnetic properties of **2–4** were measured by ESR where no evidence of ZFS was found. Pulsed-field magnetization data show that the critical fields for **1–4** vary from 5.8 to 9.4 T, which are significantly smaller than those for $[\text{Ni}(\text{HF}_2)(\text{pyz})_2]\text{Z}$ ($\text{Z} = \text{PF}_6^-$ and SbF_6^-). Taken together, the magnetic property measurements reveal the interlayer interaction can be suppressed by the choice of the X ligand. Despite the differences in the interlayer interactions, the Ni–pyz–Ni interactions in **2–4** remain largely unaltered and are found to be in the vicinity of 1 K. This result is in keeping with the prominent λ -anomaly in the heat capacity data, and excellent agreement for T_{N} was achieved between experiment and QMC predictions for **2** and **4**. The obtained J_{pyz} values are consistent with the Q1D magnetism found in the $[\text{Ni}(\text{HF}_2)(\text{pyz})_2]\text{Z}$ family. Compound **1** possesses a finite ZFS and reduced magnetic dimensionality.

This study, in combining with the previous work on the $[\text{Ni}(\text{HF}_2)(\text{pyz})_2]\text{Z}$ family, reveals that prudent ligand choice may allow systematic tuning of the interlayer interaction between $[\text{Ni}(\text{pyz})_2]^{2+}$ planes, permitting the preselection of Q1D, Q2D, and 3D magnetism.

In addition to controlling the magnetic dimensionality, lattice randomness in low-dimensional $S = 1$ antiferromagnets can lead to a highly nontrivial phase diagram.⁸¹ Such randomness can be introduced in molecule-based magnets by doping the system with diamagnetic ions, e.g., $\text{Zn}(\text{II})$, and the concentration of dopants can be controlled in the synthesis. The compounds studied in this work offer a promising opportunity for studying the effect of lattice randomness and other cooperative phenomena.

Improvements in the experimental testing of low-dimensional $S = 1$ antiferromagnets require better models for understanding the underlying physics. Specifically, a model to calculate the ordering temperature considering both the influence of the ZFS parameter D and the exchange anisotropy is strongly desired for interpreting experimental data. In addition, further DFT studies are required for a better appreciation of the mechanisms of the magnetic interactions as well as the ZFS of $\text{Ni}(\text{II})$ ion. Such studies can allow prediction of magnetic properties based on crystalline architectures. The possibility to target molecule-based magnets as effective simulators of low-dimensional magnetism is ensured by a crystal engineering approach as was demonstrated in this work. Future work on **1–4** will entail detailed neutron scattering studies

■ ASSOCIATED CONTENT

Supporting Information

The Supporting Information is available free of charge on the ACS Publications website at DOI: 10.1021/acs.inorgchem.5b02991.

Figure S1, synchrotron X-ray powder diffraction pattern and Rietveld fit for $\text{NiCl}_2(\text{pyz})_2$ (**1**); Figure S2, synchrotron X-ray powder diffraction pattern and Rietveld fit for $\text{NiBr}_2(\text{pyz})_2$ (**2**); Figure S3, synchrotron X-ray powder diffraction pattern and Rietveld fit for $\text{NiI}_2(\text{pyz})_2$ (**3**); Figure S4, synchrotron X-ray powder diffraction pattern and Rietveld fit for $\text{Ni}(\text{NCS})_2(\text{pyz})_2$ (**4**); and Figure S5, comparison of X-ray powder patterns for fitted and calculated models of $\text{NiCl}_2(\text{pyz})_2$ assuming $I4/mmm$ and $Ccca$ space group symmetries (PDF)

Crystallographic information for compound **1** (CIF)

Crystallographic information for compound **2** (CIF)

Crystallographic information for compound **3** (CIF)

Crystallographic information for compound **4** (CIF)

■ AUTHOR INFORMATION

Corresponding Author

*E-mail: jmanson@ewu.edu.

Notes

The authors declare no competing financial interest.

■ ACKNOWLEDGMENTS

Work at EWU was supported by the National Science Foundation under grant no. DMR-1306158. A portion of this work was performed at the National High Magnetic Field Laboratory, which is supported by National Science Foundation Cooperative Agreement No. DMR-1157490, the State of Florida, and the U.S. Department of Energy (DoE) and through the DoE Basic Energy Science Field Work Proposal "Science in 100 T." Work done in the UK is supported by the EPSRC. Data

presented in this paper resulting from the UK effort will be made available at <http://wrap.warwick.ac.uk/77684>. We are grateful to Alex Amato for technical assistance. Use of the Advanced Photon Source at Argonne National Laboratory was supported by the U.S. DoE, Office of Science, Office of Basic Energy Sciences, under Contract No. DE-AC02-06CH11357. Use of the National Synchrotron Light Source, Brookhaven National Laboratory, was supported by the U.S. DoE, Office of Basic Energy Sciences, under Contract No. DE-AC02-98CH10886.

REFERENCES

- (1) Haldane, F. D. M. *Phys. Lett. A* **1983**, 93 (9), 464–468.
- (2) Haldane, F. D. M. *Phys. Rev. Lett.* **1983**, 50 (15), 1153–1156.
- (3) Renard, J. P.; Verdager, M.; Regnault, L. P.; Erkelens, W. a. C.; Rossat-Mignod, J.; Stirling, W. G. *Europhys. Lett.* **1987**, 3 (8), 945–952.
- (4) Ajiro, Y.; Goto, T.; Kikuchi, H.; Sakakibara, T.; Inami, T. *Phys. Rev. Lett.* **1989**, 63 (13), 1424–1427.
- (5) Affleck, I. *Phys. Rev. B: Condens. Matter Mater. Phys.* **1991**, 43 (4), 3215–3222.
- (6) Zapf, V. S.; Zocco, D.; Hansen, B. R.; Jaime, M.; Harrison, N.; Batista, C. D.; Kenzelmann, M.; Niedermayer, C.; Lacerda, A.; Paduan-Filho, A. *Phys. Rev. Lett.* **2006**, 96 (7), 077204.
- (7) Zvyagin, S. A.; Wosnitzer, J.; Batista, C. D.; Tsukamoto, M.; Kawashima, N.; Krzystek, J.; Zapf, V. S.; Jaime, M.; Oliveira, N. F.; Paduan-Filho, A. *Phys. Rev. Lett.* **2007**, 98 (4), 047205.
- (8) Kohama, Y.; Sologubenko, A. V.; Dilley, N. R.; Zapf, V. S.; Jaime, M.; Mydosh, J. A.; Paduan-Filho, A.; Al-Hassanieh, K. A.; Sengupta, P.; Gangadharaiyah, S.; Chernyshev, A. L.; Batista, C. D. *Phys. Rev. Lett.* **2011**, 106 (3), 037203.
- (9) Orendáč, M.; Orendáčová, A.; Černák, J.; Feher, A.; Signore, P. J. C.; Meisel, M. W.; Merah, S.; Verdager, M. *Phys. Rev. B: Condens. Matter Mater. Phys.* **1995**, 52 (5), 3435–3440.
- (10) Orendáč, M.; Zvyagin, S.; Orendáčová, A.; Sieling, M.; Lüthi, B.; Feher, A.; Meisel, M. W. *Phys. Rev. B: Condens. Matter Mater. Phys.* **1999**, 60 (6), 4170–4175.
- (11) Albuquerque, A. F.; Hamer, C. J.; Oitmaa, J. *Phys. Rev. B: Condens. Matter Mater. Phys.* **2009**, 79 (5), 054412.
- (12) Bishop, R. F.; Li, P. H. Y.; Darradi, R.; Richter, J.; Campbell, C. E. *J. Phys.: Condens. Matter* **2008**, 20 (41), 415213.
- (13) Hamer, C. J.; Rojas, O.; Oitmaa, J. *Phys. Rev. B: Condens. Matter Mater. Phys.* **2010**, 81 (21), 214424.
- (14) Wierschem, K.; Kato, Y.; Nishida, Y.; Batista, C. D.; Sengupta, P. *Phys. Rev. B: Condens. Matter Mater. Phys.* **2012**, 86 (20), 201108.
- (15) Zhang, Z.; Wierschem, K.; Yap, I.; Kato, Y.; Batista, C. D.; Sengupta, P. *Phys. Rev. B: Condens. Matter Mater. Phys.* **2013**, 87 (17), 174405.
- (16) Wierschem, K.; Sengupta, P. *Phys. Rev. Lett.* **2014**, 112 (24), 247203.
- (17) Manson, J. L.; Conner, M. M.; Schlueter, J. A.; Lancaster, T.; Blundell, S. J.; Brooks, M. L.; Pratt, F. L.; Papageorgiou, T.; Bianchi, A. D.; Wosnitzer, J.; Whangbo, M.-H. *Chem. Commun.* **2006**, 2006 (47), 4894.
- (18) Čížmár, E.; Ozerov, M.; Wosnitzer, J.; Thielemann, B.; Krämer, K. W.; Rüegg, C.; Piovesana, O.; Klanjšek, M.; Horvatić, M.; Berthier, C.; Zvyagin, S. A. *Phys. Rev. B: Condens. Matter Mater. Phys.* **2010**, 82 (5), 054431.
- (19) Manson, J. L.; Schlueter, J. A.; Funk, K. A.; Southerland, H. I.; Twamley, B.; Lancaster, T.; Blundell, S. J.; Baker, P. J.; Pratt, F. L.; Singleton, J.; McDonald, R. D.; Goddard, P. A.; Sengupta, P.; Batista, C. D.; Ding, L.; Lee, C.; Whangbo, M.-H.; Franke, I.; Cox, S.; Baines, C.; Trial, D. J. *Am. Chem. Soc.* **2009**, 131 (19), 6733–6747.
- (20) Manson, J. L.; Schlueter, J. a.; McDonald, R. D.; Singleton, J. J. *Low Temp. Phys.* **2010**, 159 (1–2), 15–19.
- (21) Choi, J.; Woodward, J. D.; Musfeldt, J. L.; Landee, C. P.; Turnbull, M. M. *Chem. Mater.* **2003**, 15 (14), 2797–2802.
- (22) Lancaster, T.; Blundell, S. J.; Brooks, M. L.; Baker, P. J.; Pratt, F. L.; Manson, J. L.; Conner, M. M.; Xiao, F.; Landee, C. P.; Chaves, F. A.; Soriano, S.; Novak, M. A.; Papageorgiou, T. P.; Bianchi, A. D.; Herrmannsdörfer, T.; Wosnitzer, J.; Schlueter, J. A. *Phys. Rev. B: Condens. Matter Mater. Phys.* **2007**, 75 (9), 094421.
- (23) Woodward, F. M.; Gibson, P. J.; Jameson, G. B.; Landee, C. P.; Turnbull, M. M.; Willett, R. D. *Inorg. Chem.* **2007**, 46 (10), 4256–4266.
- (24) Goddard, P. a.; Manson, J. L.; Singleton, J.; Franke, I.; Lancaster, T.; Steele, A. J.; Blundell, S. J.; Baines, C.; Pratt, F. L.; McDonald, R. D.; Ayala-Valenzuela, O. E.; Corbey, J. F.; Southerland, H. I.; Sengupta, P.; Schlueter, J. a. *Phys. Rev. Lett.* **2012**, 108 (7), 077208.
- (25) Goddard, P. A.; Singleton, J.; Sengupta, P.; McDonald, R. D.; Lancaster, T.; Blundell, S. J.; Pratt, F. L.; Cox, S.; Harrison, N.; Manson, J. L.; Southerland, H. I.; Schlueter, J. A. *New J. Phys.* **2008**, 10 (8), 083025.
- (26) Steele, a. J.; Lancaster, T.; Blundell, S. J.; Baker, P. J.; Pratt, F. L.; Baines, C.; Conner, M. M.; Southerland, H. I.; Manson, J. L.; Schlueter, J. a. *Phys. Rev. B: Condens. Matter Mater. Phys.* **2011**, 84 (6), 064412.
- (27) Manson, J. L.; Lapidus, S. H.; Stephens, P. W.; Peterson, P. K.; Carreiro, K. E.; Southerland, H. I.; Lancaster, T.; Blundell, S. J.; Steele, A. J.; Goddard, P. a.; Pratt, F. L.; Singleton, J.; Kohama, Y.; McDonald, R. D.; Sesto, R. E. D.; Smith, N. a.; Bendix, J.; Zvyagin, S. a.; Kang, J.; Lee, C.; Whangbo, M.-H.; Zapf, V. S.; Plonczak, A. *Inorg. Chem.* **2011**, 50 (13), 5990–6009.
- (28) Manson, J. L.; Carreiro, K. E.; Lapidus, S. H.; Stephens, P. W.; Goddard, P. a.; Del Sesto, R. E.; Bendix, J.; Ghannadadeh, S.; Franke, I.; Singleton, J.; Lancaster, T.; Möller, J. S.; Baker, P. J.; Pratt, F. L.; Blundell, S. J.; Kang, J.; Lee, C.; Whangbo, M.-H. *Dalt. Trans.* **2012**, 41 (24), 7235.
- (29) Lever, A. B. P.; Lewis, J.; Nyholm, R. S. *J. Chem. Soc.* **1963**, 5042.
- (30) Lever, A. B. P.; Lewis, J.; Nyholm, R. S. *J. Chem. Soc.* **1964**, 4761.
- (31) Goldstein, M.; Taylor, F. B.; Unsworth, W. D. *J. Chem. Soc., Dalton Trans.* **1972**, 1972 (3), 418.
- (32) Otieno, T.; Thompson, R. C. *Can. J. Chem.* **1995**, 73 (2), 275–283.
- (33) James, M. *Aust. J. Chem.* **2002**, 55 (3), 219.
- (34) Wriedt, M.; Jeß, I.; Näther, C. *Eur. J. Inorg. Chem.* **2009**, 2009 (10), 1406–1413.
- (35) Wang, Q.-L.; Qi, F.; Yang, G.-M.; Liao, D.-Z.; Yang, G.-M.; Ren, H.-X. *Z. Anorg. Allg. Chem.* **2010**, 636 (3–4), 634–640.
- (36) Wang, J.; Toby, B. H.; Lee, P. L.; Ribaud, L.; Antao, S. M.; Kurtz, C.; Ramanathan, M.; Von Dreele, R. B.; Beno, M. a. *Rev. Sci. Instrum.* **2008**, 79 (8), 085105.
- (37) TOPAS V3: General Profile and Structure Analysis Software for Powder Diffraction Data Use's Manual; Coelho Software: Brisbane, Australia, 2005.
- (38) Coelho, A. A. *J. Appl. Crystallogr.* **2000**, 33 (3), 899–908.
- (39) Bachmann, R. *Rev. Sci. Instrum.* **1972**, 43 (2), 205.
- (40) Riegel, S.; Weber, G. J. *Phys. E: Sci. Instrum.* **1986**, 19 (10), 790–791.
- (41) Effect, T.-M., *The Magnetocaloric Effect and its Applications*; Condensed Matter Physics, Taylor & Francis, 2003; Vol. 6.
- (42) Blundell, S. J. *Contemp. Phys.* **1999**, 40 (3), 175–192.
- (43) Syljuåsen, O. F.; Sandvik, A. W. *Phys. Rev. E: Stat. Phys., Plasmas, Fluids, Relat. Interdiscip. Top.* **2002**, 66 (4), 046701.
- (44) Syljuåsen, O. F. *Phys. Rev. E: Stat. Phys., Plasmas, Fluids, Relat. Interdiscip. Top.* **2003**, 67 (4), 046701.
- (45) Noodleman, L. *J. Chem. Phys.* **1981**, 74 (10), 5737.
- (46) Neese, F. ORCA, Version 2.8; University of Bonn: Bonn, Germany, 2010.
- (47) Sinnecker, S.; Neese, F.; Lubitz, W. *JBIC, J. Biol. Inorg. Chem.* **2005**, 10 (3), 231–238.
- (48) Neese, F. *Coord. Chem. Rev.* **2009**, 253 (5–6), 526–563.
- (49) Yamaguchi, K.; Takahara, Y.; Fueno, T. In *Applied quantum chemistry*; Smith, V. H., Schaefer, J. H. F., III, Morokuma, K., Eds.; D. Reidel: Dordrecht, Holland, 1986; pp 155–185.
- (50) Soda, T.; Kitagawa, Y.; Onishi, T.; Takano, Y.; Shigeta, Y.; Nagao, H.; Yoshioka, Y.; Yamaguchi, K. *Chem. Phys. Lett.* **2000**, 319 (3–4), 223–230.
- (51) Weigend, F.; Ahlrichs, R. *Phys. Chem. Chem. Phys.* **2005**, 7 (18), 3297.

- (52) Carreck, P. W.; Goldstein, M.; McPartlin, E. M.; Unsworth, W. D. *J. Chem. Soc. D* **1971**, No. 24, 1634.
- (53) Gairing, C.; Lentz, A.; Große, E.; Haseidl, M.; Walz, L. Z. *Kristallogr. - Cryst. Mater.* **1996**, 211 (11), 804.
- (54) Real, J. A.; De Munno, G.; Munoz, M. C.; Julve, M. *Inorg. Chem.* **1991**, 30 (12), 2701–2704.
- (55) Lu, J.; Paliwala, T.; Lim, S. C.; Yu, C.; Niu, T.; Jacobson, A. J. *Inorg. Chem.* **1997**, 36 (5), 923–929.
- (56) Lloret, F.; Julve, M.; Cano, J.; Munno, G. De. *Mol. Cryst. Liq. Cryst. Sci. Technol., Sect. A* **1999**, 334 (1), 569–585.
- (57) Bordallo, H. N.; Chapon, L.; Manson, J. L.; Ling, C. D.; Qualls, J. S.; Hall, D.; Argyriou, D. N. *Polyhedron* **2003**, 22 (14–17), 2045–2049.
- (58) Luo, W.-X.; Yu, M.-M.; Zheng, L.; Cui, A.-L.; Kou, H.-Z. *Acta Crystallogr., Sect. E: Struct. Rep. Online* **2006**, 62 (10), m2532–m2534.
- (59) Sengupta, P.; Sandvik, A. W.; Singh, R. R. P. *Phys. Rev. B: Condens. Matter Mater. Phys.* **2003**, 68 (9), 094423.
- (60) Sorai, M.; Nakano, M.; Miyazaki, Y. *Chem. Rev.* **2006**, 106 (3), 976–1031.
- (61) The lattice contribution to the heat capacity calculated by the Debye model is proportional to T^3 , which has a powerlaw dependence similar to that of the low-temperature C_{mag} . However, they are characterized by very different energy scales and at low temperatures ($T < 2$ K) $C_{\text{mag}} \gg C_{\text{latt}}$.
- (62) Juhász Junger, L.; Ihle, D.; Richter, J. *Phys. Rev. B: Condens. Matter Mater. Phys.* **2009**, 80 (6), 064425.
- (63) Lancaster, T.; Blundell, S. J.; Brooks, M. L.; Pratt, F. L.; Manson, J. L. *Phys. B* **2006**, 374–375 (0), 118–121.
- (64) Abragam, A.; Bleaney, B. *Electron Paramagnetic Resonance of Transition Ions*, by A. Abragam and B. Bleaney; Oxford Classic Texts in the Physical Sciences, Oxford University Press: Oxford, 1970.
- (65) Park, K.; Novotny, M. A.; Dalal, N. S.; Hill, S.; Rikvold, P. A. *Phys. Rev. B: Condens. Matter Mater. Phys.* **2001**, 65 (1), 014426.
- (66) Castner, T. G.; Seehra, M. S. *Phys. Rev. B* **1971**, 4 (1), 38–45.
- (67) Nagata, K.; Tazuke, Y. *J. Phys. Soc. Jpn.* **1972**, 32 (2), 337–345.
- (68) Tazuke, Y.; Nagata, K. *J. Phys. Soc. Jpn.* **1971**, 30 (1), 285–285.
- (69) Katsumata, K. *J. Phys.: Condens. Matter* **2000**, 12 (47), R589–R614.
- (70) Wierschem, K.; Sengupta, P. *J. Phys.: Conf. Ser.* **2012**, 400 (3), 032112.
- (71) Anderson, F. B.; Callen, H. B. *Phys. Rev.* **1964**, 136 (4A), A1068–A1087.
- (72) De Jongh, L. J.; Miedema, A. R. *Adv. Phys.* **2001**, 50 (8), 947–1170.
- (73) Moriya, T. *Phys. Rev.* **1960**, 120 (1), 91–98.
- (74) Carlin, R. L.; De Jongh, L. J. *Chem. Rev.* **1986**, 86 (4), 659–680.
- (75) Schlueter, J. a.; Park, H.; Halder, G. J.; Armand, W. R.; Dunmars, C.; Chapman, K. W.; Manson, J. L.; Singleton, J.; McDonald, R.; Plonczak, A.; Kang, J.; Lee, C.; Whangbo, M.-H.; Lancaster, T.; Steele, A. J.; Franke, I.; Wright, J. D.; Blundell, S. J.; Pratt, F. L.; DeGeorge, J.; Turnbull, M. M.; Landee, C. P. *Inorg. Chem.* **2012**, 51 (4), 2121–2129.
- (76) Lapidus, S. H.; Manson, J. L.; Park, H.; Clement, A. J.; Ghannadzadeh, S.; Goddard, P.; Lancaster, T.; Möller, J. S.; Blundell, S. J.; Telling, M. T. F.; Kang, J.; Whangbo, M.-H.; Schlueter, J. a. *Chem. Commun.* **2013**, 49 (5), 499–501.
- (77) Lancaster, T.; Blundell, S. J.; Pratt, F. L.; Brooks, M. L.; Manson, J. L.; Brechin, E. K.; Cadiou, C.; Low, D.; McInnes, E. J. L.; Winpenny, R. E. P. *J. Phys.: Condens. Matter* **2004**, 16 (40), S4563–S4582.
- (78) Bordallo, H. N.; Chapon, L.; Manson, J. L.; Hernández-Velasco, J.; Ravot, D.; Reiff, W. M.; Argyriou, D. N. *Phys. Rev. B: Condens. Matter Mater. Phys.* **2004**, 69 (22), 224405.
- (79) Rastelli, E.; Sedazzari, S.; Tassi, A. J. *Phys.: Condens. Matter* **1990**, 2 (45), 8935–8944.
- (80) Yasuda, C.; Todo, S.; Hukushima, K.; Alet, F.; Keller, M.; Troyer, M.; Takayama, H. *Phys. Rev. Lett.* **2005**, 94 (21), 217201.
- (81) Roscilde, T.; Haas, S. *Phys. Rev. Lett.* **2007**, 99 (4), 047205.